

# OVERVIEW OF THE ANTARCTIC CIRCUMNAVIGATION EXPEDITION: STUDY OF PREINDUSTRIAL-LIKE AEROSOLS AND THEIR CLIMATE EFFECTS (ACE-SPACE)

JULIA SCHMALE, ANDREA BACCARINI, IRIS THURNHERR, SILVIA HENNING, AVICHAY EFRAIM, LEIGHTON REGAYRE, CONOR BOLAS, MARKUS HARTMANN, ANDRÉ WELTI, KATRIANNE LEHTIPALO, FRANZISKA AEMISEGGER, CHRISTIAN TATZELT, SEBASTIAN LANDWEHR, ROBIN L. MODINI, FIONA TUMMON, JILL S. JOHNSON, NEIL HARRIS, MARTIN SCHNAITER, ALESSANDRO TOFFOLI, MARZIEH DERKANI, NICOLAS BUKOWIECKI, FRANK STRATMANN, JOSEF DOMMEN, URS BALTENSBERGER, HEINI WERNLI, DANIEL ROSENFELD, MARTIN GYSEL-BEER, AND KEN S. CARSLAW

Aerosol characteristics over the Southern Ocean are surprisingly heterogeneous because of the distinct regional dynamics and marine microbial regimes, but satellite observations and model simulations underestimate the abundance of cloud condensation nuclei.

Sampling aerosol and trace gases on *R/V Akademik Tryoshnikov* at the Antarctic coast near the Mertz Glacier (67°09'S, 144°23'E).  
Photo credit: Julia Schmale.



**T**he World Climate Research Programme highlights the fact that “limited understanding of clouds is the major source of uncertainty in climate sensitivity, but it also contributes substantially to persistent biases in modeled circulation systems” (Bony and Stevens 2012). Investigating aerosol–cloud interactions over the Southern Ocean is a crucial step toward improving these shortcomings for two reasons. The first reason is that the Southern Ocean is the largest continuous region on Earth in which climate models exhibit a strong positive bias of surface solar radiation of between 10 and 20 W m<sup>-2</sup> (Flato et al. 2013). The bias has implications for the representation of sea surface temperature, sea ice, storm tracks, and atmospheric energy transport in climate models (Ceppi et al. 2012; Hwang and Frierson 2013; Kay et al. 2016).

A major reason for this bias is the poor representation of the persistent layer of shallow clouds in climate models, which do not reflect enough solar radiation (Bodas-Salcedo et al. 2014; Trenberth and Fasullo 2010). Stratocumulus clouds over the Southern Ocean are often mixed-phased and contain supercooled droplets (Huang et al. 2015). In mixed-phased clouds liquid droplets and ice crystals coexist. Ice crystals form on ice nucleating particles (INP) at temperatures higher than the homogeneous freezing point of water (at <-36°C), while liquid droplets form on cloud condensation nuclei (CCN). Models often produce too many ice crystals in mixed-phased clouds that consume the liquid droplets and precipitate the cloud (Kay et al. 2016). Models are hence very sensitive to INPs as demonstrated by Vergara-Temprado et al. (2018), who show that ►

the short lifetime of clouds in the cold sectors of extratropical cyclones in the model is caused by inadequate representation of natural INP and cloud microphysical processes.

The second reason why the study of Southern Ocean clouds is important is because the region still exhibits preindustrial-like aerosol properties in austral summer due to its remoteness (Hamilton et al. 2014). Currently, the lack of a well-defined baseline for preindustrial aerosol–cloud interactions introduces large uncertainty in estimates of anthropogenic radiative forcing caused by cloud albedo adjustments due to human activity (Carslaw et al. 2013). Hence, studying aerosol and cloud properties and behavior under preindustrial-like aerosol conditions is essential to reduce this uncertainty.

Fundamental questions related to the sources and processes of particles that influence cloud albedo remain open despite the number of field studies targeted at understanding gaseous chemistry, aerosol processes, and clouds in the region since the 1970s (Fig. 1, Table 1). The remoteness of the Southern Ocean and the large and heterogeneous area it covers pose a challenge to

performing in situ measurements. In situ measurements are needed to study processes that cannot be observed by satellite, such as condensation of semi-volatile species on aerosol particles or heterogeneous chemistry (cloud processing), but need to be included in models to properly represent the

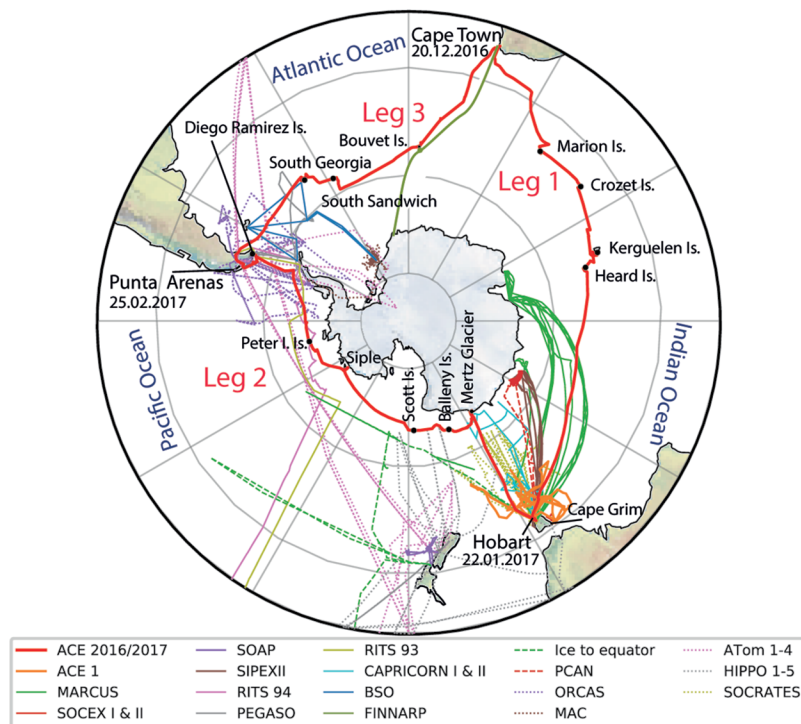


**FIG. 1. Tracks of Southern Ocean campaigns with aerosol measurement components between the 1970s and 2018. Harbor departure dates and island (Is.) stops of the ACE 2016/17 cruise (red line) are indicated. Ship tracks are represented by full lines, and flight tracks by dashed lines. See Table 1 for campaign information.**

**AFFILIATIONS:** SCHMALE, BACCARINI, LANDWEHR, MODINI, BUKOWIECKI,\* DOMMEN, BALTENSPERGER, AND GYSEL-BEER—Laboratory of Atmospheric Chemistry, Paul Scherrer Institute, Villigen, Switzerland; THURNHERR, AEMISEGGER, TUMMON, AND WERNLI—Institute for Atmospheric and Climate Science, ETH Zurich, Zurich, Switzerland; HENNING, HARTMANN, WELTI,\* TATZELT, AND STRATMANN—Leibniz Institute for Tropospheric Research, Leipzig, Germany; EFRAIM AND ROSENFELD—The Hebrew University of Jerusalem, Jerusalem, Israel; REGAYRE, JOHNSON, AND CARSLAW—Institute for Climate and Atmospheric Science, School of Earth and Environment, University of Leeds, Leeds, United Kingdom; BOLAS—University of Cambridge, Cambridge, United Kingdom; LEHTIPALO—Laboratory of Atmospheric Chemistry, Paul Scherrer Institute, Villigen, Switzerland, and Finnish Meteorological Institute, and Institute for Atmospheric and Earth System Research, and Department of Physics, Faculty of Science, University of Helsinki, Helsinki, Finland; TUMMON—Institute for Atmospheric and Climate Science, ETH Zurich, Zurich, and MeteoSwiss, Payerne, Switzerland; HARRIS—Centre for Environmental and Agricultural Informatics, Cranfield University,

Cranfield, United Kingdom; SCHNAITER—Institute of Meteorology and Climate Research, Karlsruhe Institute of Technology, Karlsruhe, Germany; TOFFOLI AND DERKANI—Department of Infrastructure Engineering, University of Melbourne, Melbourne, Victoria, Australia

\* **CURRENT AFFILIATIONS:** BUKOWIECKI—Atmospheric Sciences, Department of Environmental Sciences, University of Basel, Basel, Switzerland; TUMMON—Swiss Federal Office of Meteorology and Climatology MeteoSwiss, Payerne, Switzerland; WELTI—Finnish Meteorological Institute, Helsinki, Finland

**CORRESPONDING AUTHOR:** Julia Schmale, julia.schmale@psi.ch

The abstract for this article can be found in this issue, following the table of contents.

DOI:10.1175/BAMS-D-18-0187.1

A supplement to this article is available online (10.1175/BAMS-D-18-0187.2)

In final form 21 June 2019

©2019 American Meteorological Society

For information regarding reuse of this content and general copyright information, consult the [AMS Copyright Policy](#).

**TABLE 1. List of studies related to aerosol–cloud interactions in the Southern Ocean.**

Name	Year	Location	Objective	Reference	Platform type
<b>Cape Grim</b>	Since 1976	40°38'S, 144°43'E	Long-term monitoring of atmospheric constituents	Ayers et al. (1997)	Station
<b>BSO</b>	Oct 1992– Jan 1993	51°–76°S	British Southern Ocean cruise influence of biogenic emissions on CCN	O'Dowd et al. (1997)	Vessel
<b>RITS 93</b>	Mar 1993	53°–70°S	Radiatively Important Trace Species, atmospheric chemistry	Bates and Quinn (1997)	Vessel
<b>RITS 94</b>	Dec 1994	53°–70°S	Radiatively Important Trace Species, atmospheric chemistry	Bates and Quinn (1997)	Vessel
<b>SOCEX I and II</b>	Jul 1993, Jan–Feb 1995	40°–43°S	Southern Ocean Cloud Experiments seasonality, cloud microphysics	Boers et al. (1996), Boers et al. (1998)	Vessel
<b>ACE I</b>	Nov–Dec 1995	40°–55°S	Aerosol Characterization Experiment, atmospheric chemical processes, cloud microphysics	Bates et al. (1998)	Vessel
<b>FINNARP</b>	Nov–Dec 2004	34°–70°S	Finnish Antarctic Research Program, ultrafine aerosol characterization	Vana et al. (2007)	Vessel
<b>HIPPO</b>	Five flights between 2009 and 2011	43°–67°S	HIAPER Pole to Pole Observations, atmospheric chemical processes, cloud microphysics	Wofsy (2011)	Aircraft
<b>SOAP</b>	Feb–Mar 2012	41°–47°S	Surface Ocean Aerosol Production	Law et al. (2017)	Vessel
<b>SIPEX II</b>	Sep–Nov 2012	42°–66°S	Sea Ice Physics and Ecosystem Experiment, aerosol microphysics and chemistry, waves	Humphries et al. (2016), Kohout et al. (2014)	Vessel
<b>PEGASO</b>	Jan–Feb 2015	53°–60°S	Plankton-derived Emissions of trace Gases and Aerosols in the Southern Ocean, air–sea interactions of trace gases and aerosols	Dall'Osto et al. (2017), Fossum et al. (2018)	Vessel
<b>MAC</b>	Nov–Dec 2015	72°–78°S	Microphysics of Antarctic Clouds	O'Shea et al. (2017)	Aircraft/ station
<b>ORCAS</b>	Jan–Mar 2016	35°–75°S	O <sub>2</sub> /N <sub>2</sub> Ratio and CO <sub>2</sub> Airborne Southern Ocean Study, air–sea gas exchange, cloud microphysics	Stephens et al. (2018)	Aircraft (vessel)
<b>CAPRICORN I and II</b>	Mar 2015, Mar–Apr 2016	43°–48°S, 43°–53°S	Clouds, Aerosols, Precipitation, Radiation and Atmospheric Composition	Protat et al. (2017), Mace and Protat (2018)	Vessel
<b>ACE 2016/17</b>	Dec 2016–Mar 2017	34°–78°S	Antarctic Circumnavigation Expedition, preindustrial-like aerosol cloud interaction	This study	Vessel
<b>ATom</b>	Feb 2017 flight from New Zealand to Chile	45°–66°S	Atmospheric Tomography Mission, atmospheric chemistry	<a href="https://espo.nasa.gov/atom/content/ATom">https://espo.nasa.gov/atom/content/ATom</a>	Aircraft
<b>Ice to Equator</b>	Apr–Jun 2016	0°–65°S	Monitoring ocean change and variability along 170°W	<a href="http://www.mnf.csiro.au/Voyages/Investigator-schedules/Plans-and-summaries/2016.aspx">www.mnf.csiro.au/Voyages/Investigator-schedules/Plans-and-summaries/2016.aspx</a>	Vessel
<b>PCAN</b>	Jan–Mar 2017		Polar Cell Aerosol Nucleation	<a href="http://www.mnf.csiro.au/Voyages/Investigator-schedules/Plans-and-summaries/2017.aspx">www.mnf.csiro.au/Voyages/Investigator-schedules/Plans-and-summaries/2017.aspx</a>	Vessel
<b>SOCRATES</b>	Jan–Feb 2018	43°–67°S	Southern Ocean Clouds, Radiation, Aerosol Transport Experimental Study	<a href="http://www.eol.ucar.edu/field_projects/socrates">www.eol.ucar.edu/field_projects/socrates</a>	Aircraft, vessel
<b>MARCUS</b>	Oct 2017–April 2018	43°–67°S	Measurements of Aerosols, Radiation, and Clouds over the Southern Ocean	<a href="http://www.arm.gov/research/campaigns/amf2017marcus">www.arm.gov/research/campaigns/amf2017marcus</a>	Vessel

surface energy budget. Among these processes is also sea spray formation, the Southern Ocean being the stormiest ocean in the world (Hanley et al. 2010). The formation of secondary aerosol from biogenic gaseous emissions is another important process because the Southern Ocean is one of the most biologically active in the world (McCoy et al. 2015). Entrainment of free tropospheric air into the marine boundary layer can also influence the aerosol budget and cloud properties (Quinn et al. 2017). Understanding these processes will allow us to better simulate the CCN and INP budget over the Southern Ocean. CCN and INP are fundamental ingredients to cloud formation in addition to atmospheric dynamic processes (Reutter et al. 2009).

This paper presents an overview and first results from the Antarctic Circumnavigation Expedition: Study of Preindustrial-like Aerosol Climate Effects (ACE-SPACE) project. In this project we combined in situ measurements of aerosols and trace gases, satellite observations of cloud droplet number concentrations, and global model simulations to constrain anthropogenic radiative forcing from aerosol cloud interactions.

**ACE-SPACE STUDY DESIGN.** Measurements were conducted from December 2016 to March 2017 aboard the R/V *Akademik Tryoshnikov* between 34° and 78°S for 90 days while the ship moved from Cape Town, South Africa, through the Indian Ocean to Hobart, Australia (leg 1), via the Pacific Ocean to Punta Arenas, Chile (leg 2), and through the Atlantic Ocean back to Cape Town (leg 3, Fig. 1). Given the constant movement of the ship except for short stays (12–60 h) at islands and the Antarctic coast, the focus of ACE-SPACE was the continuous measurements of a range of aerosol and trace gas characteristics (Table 2) relevant for aerosol–cloud interactions. The in situ measurements are also used to validate satellite observations of cloud droplet number concentrations  $N_d$  and to constrain the uncertainty of aerosol parameters in the Global Model of Aerosol Processes (Mann et al. 2010) and hence the uncertainty in aerosol radiative forcing in the United Kingdom Chemistry and Aerosol (UKCA) model. Other projects on board measured complementary variables such as wave properties, marine microbial activity and precipitation (variables used for this work are listed in Table 2, an overview of all projects is provided at <http://spi-ace-expedition.ch/>).

**Specific objectives.** Measurements were designed for three principal objectives:

- (i) to capture the summertime spatial variability of the aerosol characteristics around Antarctica and the Southern Ocean;
- (ii) to provide an in situ reference, meaning spectra of CCN number concentrations, for remotely sensed cloud droplet number concentration  $N_d$ ; and
- (iii) to facilitate improved representations of preindustrial-like aerosol properties in global climate models to reevaluate the radiative forcing from aerosol–cloud interactions.

Regarding (i), the Southern Ocean is one of the regions where we know very little about aerosol properties (Hamilton et al. 2014). Geographically, most efforts have focused on specific sectors of the Southern Ocean, for example, south of Tasmania or around the Drake Passage, in the last three decades (Table 1). ACE-SPACE offered the first opportunity to study aerosol properties in the Indian, Pacific, and Atlantic Oceans in the same season. This allows comparison of aerosol properties over the open ocean in the westerly wind belt, close to the coast of Antarctica in the microbially active polynya region, and in the vicinity of sub-Antarctic islands. Polynya are large open water areas in otherwise sea-ice-covered regions. Expected differences include the relative importance of sea spray aerosol (SSA; including sea salt and organic compounds) and marine biogenic emissions for the CCN number concentration (Ayers et al. 1997; Fossum et al. 2018), the potential contribution of locally confined emissions from land-based animal colonies (Schmale et al. 2013), and occasional influence from outgassing volcanoes (Schmidt et al. 2012). Figure 2 schematically illustrates the various elements and processes that can contribute to the particle population. Based on previous cruises in the Southern Ocean, the contribution of SSA to CCN can be highly variable between 10% and 100% (Quinn et al. 2017; Fossum et al. 2018). This implies that in the absence of anthropogenic influence the oxidation products from marine emissions of dimethylsulfide (DMS), that is, non-sea-salt sulfate (nss-SO<sub>4</sub>) and methanesulfonic acid (MSA, Fig. 2) can be responsible for very large fractions of the CCN population. DMS can contribute to CCN through two different pathways (e.g., Korhonen et al. 2008): 1) DMS oxidation to sulfuric acid and formation of new particles, which can either happen in the marine boundary layer (MBL) or in the free troposphere, and 2) condensation of DMS oxidation products (i.e., MSA and H<sub>2</sub>SO<sub>4</sub>) onto preexisting smaller particles, which subsequently grow into the CCN size range (Chen et al. 2018; Hodshire et al. 2019).

**TABLE 2.** Instrumentation and measured variables on board R/V *Akademik Tryoshnikov*. All data will be available on the ACE database (<https://zenodo.org/communities/spi-ace/>). Datasets will be available within 2019. Some have restricted access until the end of 2019; thereafter, they are fully accessible. Particle sizes are given as diameters. Abbreviations are condensation particle counter (CPC), neutral cluster and air ion spectrometer (NAIS), scanning mobility particle sizer (SMPS), aerodynamic particle sizer (APS), wide-band integrated bioaerosol sensor (WIBS), chemical ionization atmospheric pressure interface time of flight mass spectrometer (CI-API-TOF), aerosol chemical speciation monitor (ACSM), cloud condensation nuclei counter (CCNC), cloud condensation nuclei (CCN), high-volume filter sampler (HVS), low-volume filter sampler (LVS), ice nucleating particles (INP), custom-built online gas chromatograph (iDIRAC), Automated Weather Station (AWS), and wave monitoring system II (WaMoSII).

Observation type	Instrument name	Measured variables	Time resolution (acquisition)
<b>Particle microphysics</b>	CPC (TSI models 3022, 3772, 3010D)	Particle number concentration with different lower cutoff (7, 10, 20 nm)	10 s
	NAIS	Particle number size distribution (2–40 nm), ion size distribution (0.8–40 nm)	3.5 min
	SMPS	Particle number size distribution (11–400 nm)	5 min
	APS	Particle number size distribution (0.5–19 $\mu\text{m}$ )	5 min
	WIBS-4	Particle number size distribution (0.5–12.5 $\mu\text{m}$ ), fluorescent particle number concentration and size	1 s
<b>Real-time chemical composition of ions, clusters, particles</b>	CI-API-TOF	Chemical composition of ions or neutral clusters	1 min
	ACSM	Submicron particulate organics, ammonium, nitrate, sulfate, chloride	30 min
	Aethalometer	Equivalent black carbon (eBC) mass concentration of total PM	1 s
<b>Hygroscopicity</b>	CCNC	CCN number concentrations (at 0.15%, 0.2%, 0.3%, 0.5%, 0.7% supersaturation)	1 s
<b>Filter-based chemical composition of particles</b>	HVS	PM <sub>10</sub> organic carbon (OC), elemental carbon (EC), water soluble organic carbon (WSOC), major ions (e.g., Na <sup>+</sup> , Cl <sup>-</sup> ), methanesulfonic acid	24 h
	LVS	PM <sub>10</sub> INP number concentrations	8 h
<b>Optical particle properties</b>	Microtops	Aerosol optical depth (AOD)	Event based
<b>Trace gases</b>	Ozone monitor (model 2BT)	O <sub>3</sub> mixing ratio	10 s
	Picarro 2401	CO <sub>2</sub> , CO, CH <sub>4</sub> , H <sub>2</sub> O mixing ratios	1 s
	iDIRAC	isoprene mixing ratio	10 min
<b>Meteorology</b>	Ship-based Vaisala AWS420 including ceilometer	Wind speed, wind direction, relative humidity, temperature, pressure, cloud-base height, radiation	30 s
<b>Waves</b>	WaMoSII	Wave height, velocity, phase, period	20 min

With regard to the second objective, satellite observations of  $N_d$  are most relevant for globally assessing the response of clouds to CCN. The relationship between surface-measured CCN and  $N_d$  determines the climatic

effects of the CCN from the ocean surface. Increasing  $N_d$  for the same cloud liquid water path increases cloud albedo (the Twomey effect; Twomey 1977). Increasing  $N_d$  for a given cloud geometrical thickness decreases

precipitation (Freud and Rosenfeld 2012). Since precipitation tends to break cloud cover of marine stratocumulus (Albrecht 1989; Rosenfeld et al. 2006; Goren and Rosenfeld 2012), added CCN increase cloud cover. Rosenfeld et al. (2019) have shown that increasing  $N_d$  for a given cloud geometrical thickness also increases the liquid water path. The combination of the effects (increased cloud albedo, cloud cover, and liquid water path) means a dramatic increase of the cloud radiative effect (Rosenfeld et al. 2019). Since  $N_d$  has such a major impact on the energy budget, it is necessary to accurately determine its driving factors. The CCN number concentration as a function of supersaturation and the base updraft determine the peak supersaturation at cloud base (Twomey 1959). However, documenting the cause and effect relationships between surface-measured CCN and  $N_d$  is very challenging due to the uncertainty in base updraft and the variable strength of the connection between the CCN near the surface and at cloud base. Therefore, addressing this question by the combined satellite and ship measurements is of major importance. For methodological reasons (see appendix B), we focus on liquid clouds. However, it is important to note that understanding mixed-phased clouds over the Southern Ocean is highly important for the regional energy balance (Mace and Protat 2018).

With respect to the third objective, much progress has been made in understanding the causes of uncertainty in state variables related to aerosol radiative forcing, such as cloud-active aerosol concentrations, precipitation, and top-of-atmosphere radiative fluxes. However, a well-constrained representation of the present-day atmosphere (influenced by anthropogenic aerosols) is insufficient to reduce uncertainty in aerosol forcing over the industrial period (Regayre et al. 2018). Processes known to cause much of the uncertainty in the preindustrial time need further investigation. These include sea spray and DMS emission fluxes, particle formation rates, and particle size distributions (Carlsaw et al. 2013; Regayre et al. 2014). A modeling study by Hamilton et al. (2014) showed that in austral summer the Southern Ocean is among the most pristine locations on Earth, with more than 29 days month<sup>-1</sup> in which the aerosol population is not directly influenced by human activity. Hence, measurements taken in this region are ideally suited to constraining preindustrial-like aerosol concentrations. Furthermore, key measurements taken during the ACE-SPACE (sea spray particle concentrations, nss-SO<sub>4</sub> concentrations, newly formed particle concentrations, and particle size distributions) can be used to constrain the most uncertain model processes that cause aerosol radiative forcing uncertainty in climate models.

*In situ measurements and remote sensing.* Table 2 gives details of the in situ instrument suite that we installed on the research vessel in a laboratory container with inlets sampling approximately 16 m above mean sea level (MSL). The link to the database is given in the table caption. More details regarding sampling line loss assessment, identification of ship exhaust periods, and instruments are provided in appendix A. Cloud droplet number concentrations were retrieved from MODIS cloud products (see appendix B).

*Modeling tools.* With the back trajectories calculated using the Lagrangian analysis tool LAGRANTO (Wernli and Davies 1997; Sprenger and Wernli 2015) based on wind fields from the operational analysis data of the European Centre for Medium-Range Weather Forecasts (ECMWF), we determined the airmass history for interpretation of the in situ results. In the supplementary material we provide an animation of airmass trajectories for every hour of the expedition.

Measurements are compared to output from version 8.4 of the UKCA model, which is a whole-atmosphere chemistry and aerosol model embedded within the HadGEM3 host model (O'Connor et al. 2014). Within the UKCA model the evolution of particle size distribution and size-resolved chemical composition of aerosols in seven size and composition modes are calculated using the Global Model of Aerosol Processes model (GLOMAP-model; Mann et al. 2010). Here we compare measurements to the mean output from perturbed parameter ensembles of the UKCA model (Yoshioka et al. 2019, manuscript submitted to *J. Adv. Model. Earth Syst.*). In these ensembles multiple uncertain aerosol and physical atmosphere parameters were perturbed simultaneously to produce a set of model variants that spans the model behavior and can be used to quantify the value of measurements as constraints on model uncertainty. More details on both models are given in appendix C.

## ENVIRONMENTAL CONDITIONS DURING THE CRUISE.

Figure 3a shows the climatological wind speed from the ERA-Interim dataset (Dee et al. 2011) at 10-m altitude for December–March from January 1979 to February 2017. The actual wind conditions encountered during ACE-SPACE are overlain. To check the comparability of the ECMWF product and the measured wind, we correlated the hourly values for the expedition at 30 m height and found a correlation coefficient of  $R^2 = 0.83$  and a slope of 1.12 (with higher measured values). For details, see appendix C.

The temporal and spatial variability of wind speeds encountered during the expedition is much

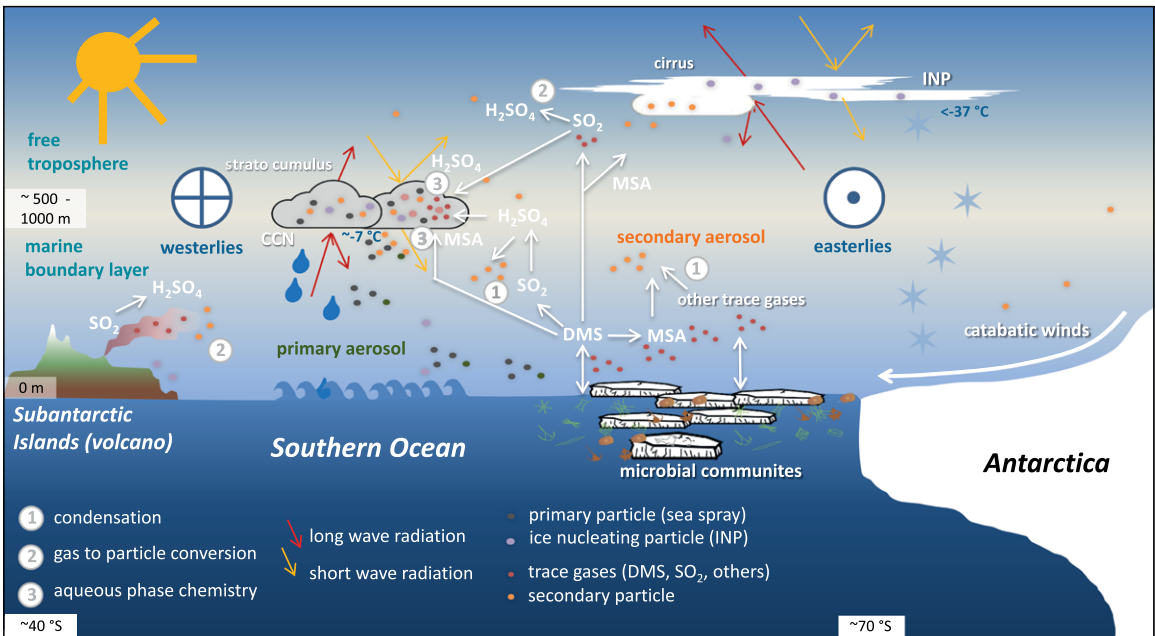


**FIG. 2. Schematic of summertime aerosol processes over the Southern Ocean. Individual processes are described in the text. Latitudes, heights, and temperatures are only indicative.**

larger than reflected by the 38-yr climatology. Individual sections, especially in the westerly wind belt between 70° and 130°E (leg 1) and 30°W and 10°E (leg 3), as well as most of leg 2, were calmer than expected from climatology. One contributing factor might be the avoidance of storms by the expedition. However, the median wind speeds of legs 1 and 3 are similar to the climatological mean.

Especially within the high wind belt, frontal systems are frequently expected (Papritz et al. 2014), which can impact the aerosol population, for example, through precipitation. During leg 1, warm-air advection dominated (60% of all instances), whereas cold-air advection was more frequent during legs 2 and 3 with 80% and 85% of the time, respectively.

Sea ice conditions were mostly relevant during leg 2, because the other legs passed well north of the main sea ice regions (Fig. 3b). Compared to climatology (Turner et al. 2017; Schlosser et al. 2018), there was significantly less ice in the Amundsen Sea (around 120°W near the Siple region), but more near the Mertz area (approximately 150°E). In fact, the spring–summer season 2016/17 showed unusual warming of the Southern Ocean by up to 1°C compared to the 2010–15 average (<https://data.giss.nasa.gov/gistemp/maps/>), which might have had some impact on sea spray production and biological activity.

The Southern Ocean is known for its high waves, caused by strong surface winds and large fetch (Hanley et al. 2010). Figure 3b compares the measured significant

wave height  $H_s$  with the corrected December–March climatological significant  $H_s$  from 2001 to 2018 from the joint CNES/NASA satellite oceanography mission series *Jason-1* and *Jason-2* (Young 1998). The former was launched in December 2001 and decommissioned in July 2013, while the latter is an ongoing follow-on mission launched in June 2008. Averages are computed in grid points of 0.5° resolution. The open-ocean legs 1 and 3 are characterized by similar  $H_s$  with a measured median of 5.5 m and an interquartile range (IQR) between 4 and 7 m. The climatological mean suggests  $H_s$  around 4.5 m and is hence slightly lower than that encountered during ACE-SPACE. Leg 2, south of the westerly wind belt, saw a median  $H_s$  of 2.5 m. The breaking of waves is the main driver behind sea spray production. During breaking, which is induced when  $H_s$  is larger than one-seventh of the wavelength, air bubbles are entrained into the water that subsequently rise to the surface and either eject jet droplets or spray from collapsing cavities (Monahan et al. 1986).

In addition to the physical conditions described above, we present in Figs. 3c and 3d the MODIS-retrieved concentration of chlorophyll-a during February 2017 and the climatological mean between 2002 and 2016 based on MODIS *Aqua* observations (Johnson et al. 2013). Generally, we encountered the expected pattern of blooms, meaning lower activity in the leg 1 region and more intense blooms during leg 2. A direct comparison for leg 2 is difficult due to the cloud coverage (white areas in Fig. 3d). Leg 3

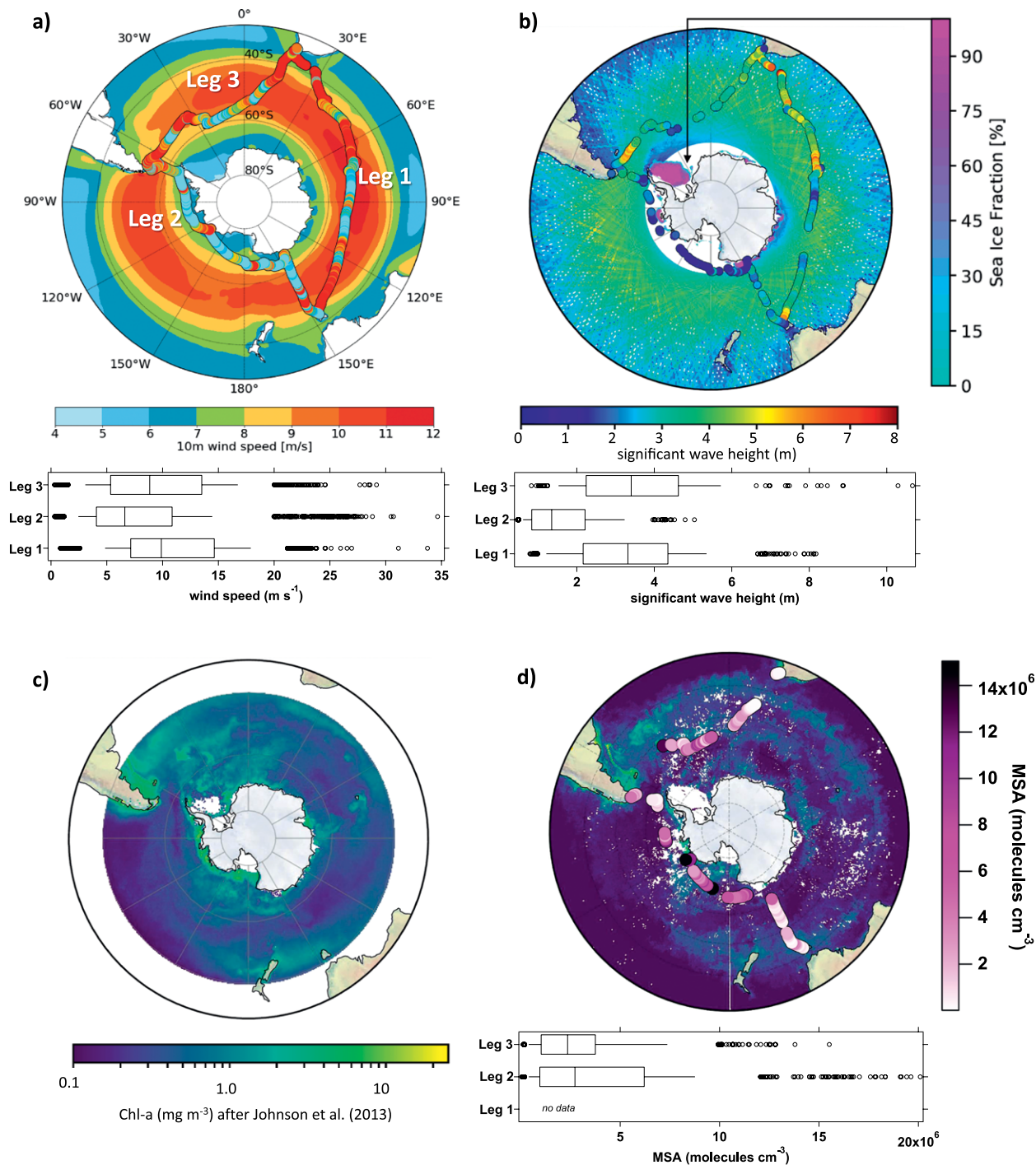


**FIG. 3.** Climatological mean values for December–March of (a) 10-m wind speed, (b) wave height and sea ice extent, and (c) chlorophyll-a (Chl-a). Wind speeds are based on the 1979–2017 ERA-Interim climatology. The measured wind speed during the cruise is plotted along the track, and box-and-whisker plots at the bottom of the panel summarize each leg. They denote the mean, interquartile range, 10th and 90th percentiles, and data points in the outer 2.5th percentiles. The significant wave height is based on radar altimeter data from the CNES/NASA oceanography mission series *Jason-1* and *Jason-2* for the years 2001–18. Measurements from the cruise are overlain and box plots are provided. Additionally, sea ice extent from MODIS is shown for 31 January 2017 (color scale on the right). In (c) the MODIS chlorophyll-a climatology covers DJFM between 2002 and 2016. (d) The chlorophyll-a concentrations for February 2017 [MODIS, same color scale as in (c)] and MSA in situ concentrations including boxplot.

saw less activity than the climatological mean, likely because it was relatively late in the season (March). Chlorophyll-a is a direct indication for the presence of phytoplankton but cannot be used to directly infer the amount of DMS released into the atmosphere, which can subsequently be oxidized to  $\text{H}_2\text{SO}_4$  or MSA (Fig. 2). We show the concentration of gaseous MSA in Fig. 3d. The highest localized concentrations were found during leg 2 in the polynya near the Siple region and leg 3 southwest of the Sandwich Islands. Note that high atmospheric MSA concentrations are not necessarily expected in the same location of high marine chlorophyll-a or DMS concentrations because of atmospheric transport and transformation processes. The atmospheric lifetime of

DMS (MSA) in the Southern Ocean is estimated to vary between 2 and 5 days (2–6 days), calculated as the ratio of the mean atmospheric burden by the sum of loss processes (Chen et al. 2018). We find enhanced MSA concentrations in the immediate vicinity of regions with elevated chlorophyll-a concentrations and along trajectories that traveled above such regions.

Transport of anthropogenic emissions to the Southern Ocean is another environmental condition that we need to consider to understand in how far our observations during ACE-SPACE are preindustrial-like. Figure 4 shows the concentrations of equivalent black carbon (eBC) and CO as a function of latitude and indicates the location of the visited ports. Elevated concentrations of these two tracers can represent anthropogenic emission influence. Concentrations for both tracers reach their background levels south of  $55^\circ\text{S}$ :  $19.2 \text{ ng m}^{-3}$  eBC and  $23.2 \text{ ppb}$  CO. For comparison, eBC concentrations at the high alpine observatory Jungfraujoch 3,500 m MSL in the Swiss Alps, which represent the remote European atmosphere, are generally  $>50 \text{ ng m}^{-3}$  during not specifically polluted conditions (Cozic et al. 2007).

**PARTICLE NUMBER, CLOUD CONDENSATION NUCLEI, AND ICE NUCLEATING PARTICLE CONCENTRATIONS.** Aerosol properties varied substantially over the Southern Ocean, and each leg exhibited distinct characteristics (Table 3). Total particle number concentrations with a lower cutoff diameter of  $7 \text{ nm}$   $N_7$  ranged between

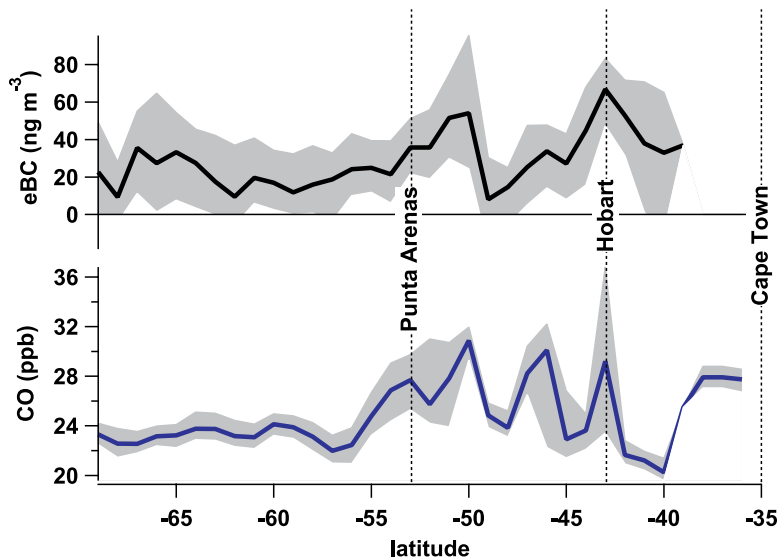


**FIG. 4.** Concentrations of the anthropogenic tracers eBC and CO as functions of latitude. Solid lines indicate the median values, and the shaded area the interquartile range. The dotted vertical lines indicate the latitudinal locations of the ports visited.

10 and  $>1,000 \text{ cm}^{-3}$  (Fig. 5). For reference, over the summer Arctic Ocean concentrations vary in a broader range between 1 and  $<4,000 \text{ cm}^{-3}$ , however with a smaller median concentration (measured with the same instrument during the Arctic Ocean 2018 expedition). Concentrations in urban areas are usually between  $10^4$  and  $10^5 \text{ cm}^{-3}$  [e.g., Wang et al. (2013) for Beijing and Pikridas et al. (2015) for Paris]. Leg 1 saw the highest median concentration with  $470 \text{ cm}^{-3}$ , followed by leg 3 with  $350 \text{ cm}^{-3}$  and leg 2 with  $280 \text{ cm}^{-3}$ . Importantly, CCN activating at a supersaturation of 0.2% ( $\text{CCN}_{0.2}$ ) do not follow the same pattern. Median concentrations are nearly the same for legs 1 and 2 ( $114$  and  $111 \text{ cm}^{-3}$ ) and slightly lower for leg 3 ( $90 \text{ cm}^{-3}$ ). These values are significantly higher than in the Arctic and slightly lower than at Mace Head (Schmale et al. 2018). Figure 6 provides the  $\text{CCN}_{0.2}$  concentration (Fig. 6b) and the activation ratio (Fig. 6c), defined as the CCN concentration divided by the total particle number concentration  $N_7$  along the track. The activation is higher in leg 2 and can be explained with larger particles (see Fig. 6a) and possibly also differences in chemical composition.

Concentrations of INP at  $-15^\circ\text{C}$  ( $\text{INP}_{-15}$ ; Fig. 5) ranged between the detection limit ( $0.1 \text{ m}^{-3}$ ) and  $54 \text{ m}^{-3}$  accounting for all measured values. The detection limit is  $0.1$ – $0.2 \text{ m}^{-3}$  depending on the sampled volume of air. The median values per leg are  $<1 \text{ m}^{-3}$ , with leg 3 having the smallest INP concentrations. For reference, INP concentrations at Mace Head in Ireland are also around  $1 \text{ m}^{-3}$  during clean conditions (McCluskey

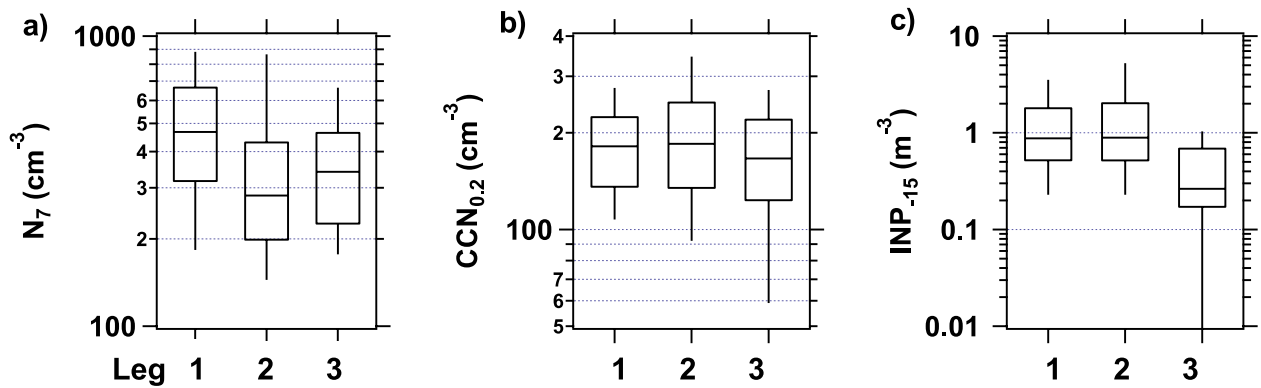


**FIG. 5.** Number concentrations of different particle types: (a) total particle number concentrations  $>7$  nm ( $N_7$ ), (b)  $CCN_{0.2}$ , and (c)  $INP_{-15}$  at  $-15^\circ\text{C}$  for each leg. The box-and-whisker plots show the median, interquartile range, and 10th and 90th percentiles.

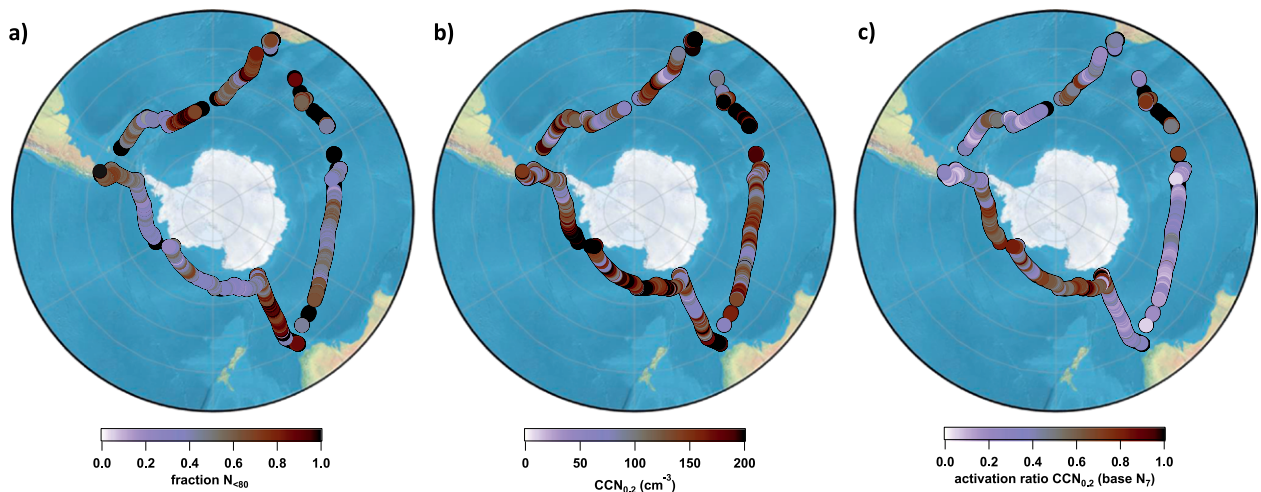


**FIG. 6.** Aerosol characteristics along the ship track: (a) fraction of particles with diameters lower than 80 nm compared to particles greater than 7 nm, (b)  $CCN_{0.2}$  concentration, and (c) ratio of  $CCN_{0.2}$  over  $N_7$ .

et al. 2018b). Legs 1 and 2 show very similar distributions of  $INP$  number concentrations even though they represent two very different environments. Comparing our results to the survey from Bigg (1973) of  $INP_{-15}$  concentrations between  $80^\circ\text{E}$  and  $140^\circ\text{W}$ , we find concentrations lower by two orders of magnitude. Newer data from McCluskey et al. (2018a) between Tasmania and  $53^\circ\text{S}$  from the CAPRICORN campaign (Table 1) compare well with ours. Their measurements had an approximate limit of detection of  $1\text{ m}^{-3}$  for  $INP_{-15}$ . The discrepancies between the recent measurements and in the 1970s are currently under investigation.

**PARTICLE SIZE, HYGROSCOPICITY, AND AIRMASS ORIGIN.** To interpret the  $CCN$  concentrations, particle size and hygroscopicity (water affinity), airmass history, and cloud processing information are needed. We show aggregated data of leg

2 (Fig. 7) as an example for the type of information that can be extracted from the ACE-SPACE dataset that includes the particle size distribution, an estimate of the cloud supersaturation and the particle hygroscopicity. Figure 7a shows  $k$ -means-based clusters of particle size distributions (run with 1,000 iterations). The figure also shows the airmass history associated with each cluster (Figs. 7b–d). For each hour of leg 2 in which a certain cluster occurred, we released 21 trajectories at different levels below 850 hPa. This pressure level roughly represents the MBL height. We counted the number of trajectories per cluster that passed through bins of  $0.5^\circ$  latitude and 10-hPa altitude. Figures 7b–d hence provide a longitudinally integrated information about the statistical distribution of the airmass origin during the previous 5 days. They allow for interpretation of particle processing rather than emission sources.

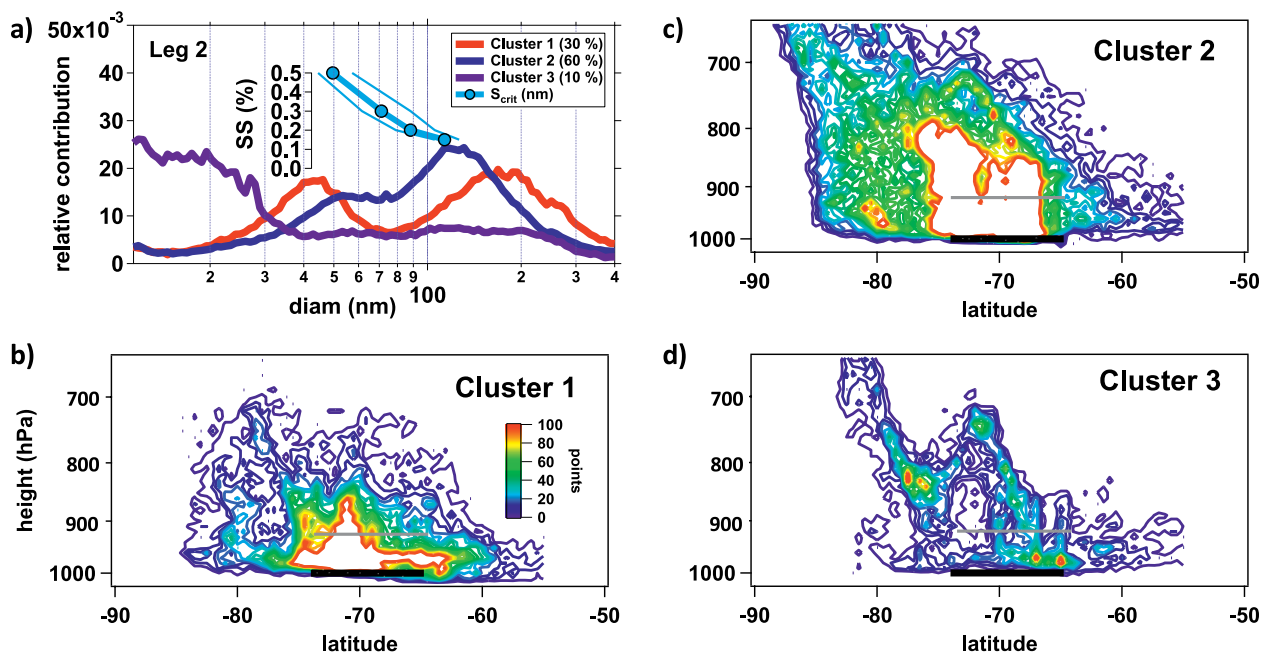


**FIG. 7.** Clustered particle size distributions of leg 2 and 5-day airmass back trajectories. (a) Normalized size distribution clusters. The inset shows the supersaturation median and interquartile range as a function of the critical diameter for leg 2. (b)–(d) Contour plots of back trajectories for clusters 1, 2, and 3, respectively, are plotted as the zonal sum (crossings) as a function of latitude and altitude. The black line indicates the latitude band of the ship track, and the gray line the approximate average cloud-base level.

The aerosol size distribution for cluster 1 features a pronounced Hoppel minimum (Hoppel and Frick 1990), a signature of cloud processing. It can reflect the scavenging of smaller Aitken mode particles into cloud droplets, which subsequently accrue mass through the aqueous phase oxidation of volatile gases such as  $\text{SO}_2$  (originating from DMS oxidation) into less volatile  $\text{H}_2\text{SO}_4$ , leaving larger accumulation mode particles behind if the cloud evaporates. The Hoppel minimum diameter ranges between 70 and 78 nm, which is distinctly larger than the Hoppel minimum diameters of the other legs (Table 3), see also Fig. 6a for the small fraction of particles with a diameter smaller than 80 nm  $N_{<80}$  during leg 2. Such a difference can reflect both varying cloud supersaturations across the Southern Ocean regions and different particle chemical composition, and hence different particle hygroscopicity. Higher hygroscopicity will move the Hoppel minimum to lower diameters for a fixed supersaturation, while higher supersaturations for the same particle hygroscopicity has the same effect on the Hoppel minimum. The median and interquartile range of the critical particle diameter, above which they act as CCN at different supersaturations during leg 2 are shown as an inset in Fig. 7. Comparing the location of the Hoppel minimum with the supersaturation–activation curve suggests

that cloud peak supersaturation was on average 0.28% during leg 2.

The back trajectories indicate that particles of the cluster 1 size distribution are associated with MBL and lower tropospheric airmasses that move along the latitudes of the cruise track. The altitude range of the trajectories is consistent with the MBL height predicted by ECMWF (about 660 m or roughly 930 hPa), which is similar to the height of the lowest cloud level measured by the ship-based ceilometer (500 m, Table 3). The fact that clouds are mostly within the MBL supports the hypothesis that cloud processing shapes the particle size distribution at the surface.

The airmass history for cluster 2 is different. A much stronger signature comes from more southerly latitudes and higher altitudes, indicating that particles might have arrived with airmasses that traveled over Antarctica and the polynya region. Cluster 2 represents the most common size distribution of the leg (60% of the time) and is associated with the cold sector of frontal systems. There is also evidence of a Hoppel minimum, which appears to be obscured by Aitken mode particles growing into the pronounced accumulation mode by other processes than exclusively cloud processing. The Aitken mode likely represents different stages of particle growth linked to the availability of condensable matter, for

example, from marine biological emissions (Fig. 3d), while the accumulation mode is likely a result of cloud processing and sea spray emission.

Cluster 3, which occurs 10% of the time, represents nucleation mode particles that were formed from gas to particle conversion. Few particles of larger sizes are present in this cluster, indicating a relatively low condensation sink for condensable species. This cluster corresponds almost entirely to two pronounced new particle formation episodes that happened in the vicinity of the Mertz glacier (Fig. 1). This is reflected by the distribution of back trajectories (Fig. 7d) which are much less spread in latitude and altitude compared to the other clusters. Trajectories show a clear MBL influence with a contribution from free tropospheric airmasses that traveled over Antarctica. Measurements of the ion size distribution down to

0.8 nm (not reported here as it will be used for a specific paper focused on new particle formation) point out that nucleation happened locally. Therefore, we can exclude a contribution of downward transported particles formed in the free troposphere. Previous research in the Southern Ocean has shown that nucleation mode particles can be entrained from aloft (Clarke et al. 1998) and down-mixed after cold-frontal passages (Gras et al. 2009). Observations of new particle formation around the Antarctic coast are very sparse and a clear understanding of the processes involved is still missing. In a single case ultrafine particles were linked to airmasses arriving from Antarctica, that is, northward air motion over sea ice (Humphries et al. 2015) but most other studies report open-ocean influence which drives coastal new particle formation (NPF; Weller et al. 2015; Jokinen

**TABLE 3. Key aerosol and trace gas properties per leg. Numbers are medians and interquartile ranges (IQR) are given in brackets.  $N_7$  refers to all particles larger than 7 nm measured by the condensation particle counter,  $N_{<80}$  refers to the number of particles with a diameter smaller than 80 nm,  $CCN_{0.2}$  is CCN that activates at 0.2% supersaturation, and  $INP_{-15}$  is INP that produces ice crystals at  $-15^\circ\text{C}$ .**

Property	Leg 1	Leg 2	Leg 3
$N_7$ ( $\text{cm}^{-3}$ )	470 [320, 665]	280 [200, 430]	350 [225, 460]
SSA concentration ( $\text{cm}^{-3}$ )	151 [73, 253]	28 [11, 72]	89 [41, 174]
SSA mode contribution to total integrated size distribution (%)	10 [7, 15]	9 [5, 14]	10 [5, 16]
$CCN_{0.2}$ ( $\text{cm}^{-3}$ )	114 [80, 140]	111 [80, 150]	90 [65, 125]
Activation ratio $CCN_{0.2}$ based on $N_7$ (%)	25 [15, 39]	51 [27, 65]	37 [19, 48]
SSA mode contribution to CCN (%)	SS = 0.15%	SS = 0.15%	SS = 0.15%
	32 [23, 55]	19 [11, 32]	30 [18, 51]
	SS = 1.0%	SS = 1.0%	SS = 1.0%
	16 [10, 22]	11 [6, 16]	16 [9, 25]
Hoppel minimum diameter [range] (nm)	48 [44, 53]	74 [70, 78]	68 [51, 82]
Contribution of $N_{<80}$ (%)	51 [42, 64]	47 [36, 63]	55 [39, 71]
$INP_{-15}$ ( $\text{m}^{-3}$ )	0.87 [0.52, 1.79]	0.89 [0.52, 2.02]	0.26 [0.17, 0.69]
First cloud level (m)	590 [330, 918]	500 [225, 855]	610 [291, 927]
ECMWF boundary layer height (m)	851 [648, 1252]	660 [340, 913]	807 [592, 1127]
MSA gaseous (molecules $\text{cm}^{-3}$ )	—	$2.7 \times 10^6$ [ $1.0 \times 10^6$ , $6.2 \times 10^6$ ]	$2.4 \times 10^6$ [ $1.0 \times 10^6$ , $3.7 \times 10^6$ ]
$\text{H}_2\text{SO}_4$ gaseous (molecules $\text{cm}^{-3}$ )	—	$2.6 \times 10^6$ [ $1.7 \times 10^6$ , $3.7 \times 10^6$ ]	$2.1 \times 10^6$ [ $1.3 \times 10^6$ , $3.7 \times 10^6$ ]
Particulate MSA ( $\mu\text{g m}^{-3}$ )	0.13 [0.08, 0.18]	0.17 [0.08, 0.23]	0.08 [0.06, 0.10]
Particulate sodium ( $\mu\text{g m}^{-3}$ )	3.94 [2.88, 5.41]	1.75 [1.03, 2.88]	2.74 [2.02, 4.28]
Particulate chloride ( $\mu\text{g m}^{-3}$ )	6.40 [4.80, 9.05]	2.60 [1.67, 4.87]	4.59 [3.28, 7.41]
Temperature ( $^\circ\text{C}$ )	6.1 [4.5, 10.2]	-0.1 [-0.9, 3.1]	3.2 [1.3, 9.5]
Wind speed ( $\text{m s}^{-1}$ )	9.88 [7.14, 14.63]	6.62 [4.07, 10.86]	8.85 [5.34, 13.51]
Significant wave height (m)	3.3 [2.2, 4.3]	1.4 [0.8, 2.2]	3.4 [2.2, 4.6]

et al. 2018), consistent with our observations. In particular, Jokinen et al. reported for the first-time molecular-level characterization of NPF in Antarctica showing that sulfuric acid–ammonia ion induced nucleation is the predominant NPF mechanism in Queen Maud Land (Aboa station).

**THE ROLE OF SEA SPRAY FOR CCN.** Sea spray formation is a key process that influences the aerosol properties significantly in some regions of the Southern Ocean. Bubbles that burst at the ocean surface as a result from air entrained into the water through wave breaking (Monahan et al. 1986) are the most important mechanism to generate sea spray. Sea spray droplets evaporate once in the air and leave behind aerosol particles that consist of a mixture of sea salt and organic particles, the latter are enriched in the sea surface micro layer (Quinn et al. 2014). Wind, which drives wave formation, is one of the key factors for sea spray aerosol (SSA) generation. This is particularly important in the Southern Ocean, where wind–wave interactions are a dominant feature (Hanley et al. 2010). We use the term SSA to refer to sea salt and primary organic aerosol stemming from the ocean.

We applied the three mode fitting algorithm after Modini et al. (2015) to the joint SMPS and APS size distributions to derive an estimate of sea spray contribution to the total particle concentration and CCN at all supersaturations. The mode diameter of the fitted SSA size distribution was constrained to lie within  $\pm 20\%$  of 180 nm to be consistent with the breaking-wave size distribution measurements of Prather et al. (2013), yielding a correlation coefficient of 0.75 between fitted SSA and filter-based  $\text{Na}^+$  mass concentrations. We estimate that the uncertainty in the 15-min median fitted-SSA number concentrations is  $\pm 50\%$  based on a sensitivity analysis to the choice of constrained mode diameter over the range 140–300 nm. SSA was similarly important for the total particle number concentration of the integrated joint particle size distribution in legs 1 and 3 with a median contribution of 10%, followed by leg 2 with 5% median contribution (Table 3). The SSA contribution to CCN for supersaturations up to 0.3% was up to 100% in extreme cases ( $< 2.3\%$  of all 15-min-averaged data points), for higher supersaturations, contributions of 80% were not exceeded. Generally, the contribution of SSA to CCN across all supersaturation is highest for leg 1, followed by leg 3, and then leg 2. Table 3 provides the contribution of SSA to CCN at 0.15 and 1.0% supersaturation for each leg. The results are in agreement with the wind speed and wave observations that suggest higher SSA production during legs 1 and 3 (Figs. 3a,b). Chemical

information from the 24-h particulate matter with a diameter  $< 10 \mu\text{m}$  ( $\text{PM}_{10}$ ) filter samples confirms this observation: the average sodium chloride mass of leg 1 is 1.3 and 2.1 times higher than in legs 3 and 2, respectively. Our SSA contribution estimate is similar to recent measurement-based calculations of SSA mode contributions south of  $60^\circ\text{S}$  using also the fitting method after Modini et al. (2015). Quinn et al. (2017) found an average SSA contribution of 15% to the total particle number concentration and between 20% and 40% to CCN for supersaturations between 1% and 0.1%, respectively. Our average SSA contributions are 11% to  $N_7$  and 16% to  $\text{CCN}_{1.0}$  and 35% to  $\text{CCN}_{0.15}$ . Note that Quinn et al. (2017) estimates are based on a smaller sector of the Southern Ocean from the RITS93 and 94 campaigns (Table 1, Fig. 1). Leg 2 of ACE-SPACE was frequently characterized by airmasses from Antarctica, hence the contribution of SSA is expected to be lower there (10% were observed). In addition, the ocean was partly covered by sea ice (Fig. 3b) and the median wind speed ( $6 \text{ m s}^{-1}$ ) was lower than during leg 1 ( $10 \text{ m s}^{-1}$ ) and leg 3 ( $8 \text{ m s}^{-1}$ ; Fig. 3a).

### **COASTAL ANTARCTIC CCN: UNRESOLVED FORMATION MECHANISMS.**

The fraction of particles serving as CCN was higher near the coast of Antarctica (Fig. 6c), in agreement with results from the large accumulation mode over coastal waters. We hypothesize that this mode compared to the rest of the cruise could be a result of two factors: 1) mass acquisition through multiple cycles of cloud processing and/or 2) the comparatively higher availability of condensable gases originating from marine microbial activity. With respect to the first factor,  $\text{SO}_2$  (a DMS oxidation product) can either be oxidized to sulfuric acid in the gas phase or through aqueous phase reactions in cloud droplets (Fig. 2), whereby heterogeneous oxidation is the faster reaction (Chen et al. 2018). The pronounced Hoppel minimum suggests that particulate sulfate formation takes place in the droplets. In this case, the marine emissions grow CCN so that lower supersaturations are sufficient to form droplets. The larger accumulation mode particles in leg 2 might result from multiple processing cycles of dissipating and condensing clouds. Being close to Antarctica on leg 2, we observed more cold and dry air outbreaks than on the other legs. The entrainment of dry air might cause clouds to dissipate more often before they precipitate their CCN. In fact, katabatic winds have been demonstrated to sublimate a significant fraction of falling snow (Grazioli et al. 2017). And, over the Antarctic Peninsula, bursts of CCN have been observed after cloud evaporation (Saxena 1996).

Regarding the second factor, air masses associated with leg 2 accumulation mode clusters traveled over chlorophyll-rich regions (Figs. 3c,d and Figs. 7b,c) from where DMS might be emitted and oxidized into MSA and  $\text{SO}_2$ . Here again, the faster oxidation path of DMS to MSA is via heterogeneous reactions (Chen et al. 2018). The 75th-percentile concentration of gaseous MSA was significantly higher during leg 2 compared to leg 3 (Table 3 and Fig. 3d); observations are not available from leg 1. Gaseous sulfuric acid (median) was also slightly higher in leg 2 compared to leg 3 (Table 3). The formation rates of MSA and sulfuric acid from DMS are a function of temperature, with colder temperatures favoring the formation of MSA (Seinfeld and Pandis 2006). This is consistent with the colder temperatures near Antarctica and the higher 75th-percentile ratio of MSA to  $\text{H}_2\text{SO}_4$  in leg 2 compared to leg 3.

As speculated, both gases ( $\text{H}_2\text{SO}_4$  and MSA) could grow the particles either through direct condensation in the gas phase or via heterogeneous chemistry inside the clouds. For a quantitative analysis of this process, in situ measurements of size-resolved MSA partitioning, in-cloud chemical evolution of particles, and cloud formation and dissipation cycles are needed.

The enhanced concentrations of trace gases, particularly MSA, are reflected in the contribution of particulate MSA to the particle population. It is 2.5 times higher in leg 2 compared to legs 1 and 3 based on the  $\text{PM}_{10}$  filter analysis. The chemical composition of particles is important because it influences their hygroscopicity and potential to become a CCN. Hygroscopicity can be expressed by the kappa value (Petters and Kreidenweis 2007) that relates a particle's dry diameter with the critical supersaturation at which it can activate as droplet. The higher the kappa value the more readily a particle can become CCN. The bulk kappa value for leg 2 has been calculated following the kappa-Köhler equation (Petters and Kreidenweis 2007). It is 0.59 and reflects the contribution of various compounds. Kappa values of MSA have rarely been reported in the literature. We use the hygroscopic growth factor at  $\text{RH} = 90\%$  of 1.57 reported by Johnson et al. (2004) and calculate a kappa value of 0.32 based on a water activity of 0.9 [see Eq. (2) in Petters and Kreidenweis (2007)]. A pure sea salt contribution to CCN would result in kappa  $\sim 1.1$  (Zieger et al. 2017) and pure sulfuric acid contribution in  $\sim 0.70$  (Schmale et al. 2018). Similar observations of decreased hygroscopicity, compared to sea salt or sulfuric acid, with higher particulate MSA fraction have been made at the Antarctic coastal station Aboa (Asmi et al. 2010).

Considering that CCN concentrations in leg 2, which were not SSA dominated, are at least as high as in the open-ocean legs, it seems that a combination of multiple cloud processing cycles and increased availability of DMS oxidation products led to particle sizes large enough to act as CCN. This counteracts the lower particle hygroscopicity through MSA addition and reduces the importance of sea spray. While previous studies have shown that  $N_d$  are associated with elevated chlorophyll-a concentrations (McCoy et al. 2015), the actual mechanisms leading to this correlation remained unclear. McCoy et al. (2015) used the particulate sulfate concentration and organic mass fraction obtained from model simulations to explain more than 50% of the spatial  $N_d$  variability (retrieved from satellite observations) and estimated that marine biological activity may be responsible for a doubling of  $N_d$  in summer. Proposed explanations include that marine surfactants enhance the SSA fraction of aerosols between 50 and 200 nm (Prather et al. 2013), which are most relevant for the CCN number concentration. With regard to leg 2, this seems unlikely to be a major contributing factor due to the small influence of SSA that we estimate. A further suggestion was that ocean-derived particulate organics have surfactant characteristics that can reduce the surface tension and hence lower the critical diameter (O'Dowd et al. 2004; Ovadnevaite et al. 2017). Our clustered size distributions show that the Hoppel minimum occurs at larger diameters closer to Antarctica. Quinn et al. (2017) predicted that SSA contributes a significant proportion of the Southern Ocean MBL CCN budget, between 30% and 40%, at supersaturations smaller than 0.3%. This means that they ascribed roughly 40% of CCN to surface sources while the origin and formation mechanisms of the remainder, that is, accumulation mode, remained unresolved.

From our data, it appears likely that accumulation mode particles grew through cloud processing; a mechanism that is potentially enhanced due to cloud formation and dissipation cycles in combination with the increased availability of condensable gases, that is, MSA and  $\text{H}_2\text{SO}_4$ . However, the question remains as to which pathways lead to the addition of MSA and  $\text{H}_2\text{SO}_4$  to the particle mass.

## COMPARISON OF REMOTE SENSING AND IN SITU OBSERVATIONS OF CLOUD CONDENSATION NUCLEI.

Even though our in situ observations are representative of what would be expected from climatological conditions, they only cover a limited amount of time (summer) and space (cruise track). Using satellite observations to retrieve  $N_d$  to the extent that they reflect the actual CCN

number concentration enables the community to create a dataset that reflects spatial and multiannual variability (see appendix B for details). Such a dataset is important to improve our estimates of radiative forcing from pristine aerosol–cloud interactions. We identified 73 satellite overpasses of the ACE-SPACE ship track with valid CCN measurements from the ship, when only shallow (up to 800 m) liquid clouds were sampled. For each case we have calculated  $N_{d^*}$ , the updraft and the supersaturation at cloud base and matched the CCN concentration at the same supersaturation from a CCN spectrum measured on the ship 2 h before and after the satellite overpass. (Fig. 8). It shows that generally the  $N_{d90}$  (the 90th percentile) concentration observed by MODIS is smaller than the measured CCN at the determined cloud-base supersaturation. Most points fall within the triangle below the 1:1 line of satellite versus ship-based measured CCN—the cloud-base-retrieved CCN is mostly lower than ship measured CCN. This means that for most of the cases the source of CCN is associated to the surface rather than to entrainment of particles from the free troposphere. A dominant free-tropospheric source would incur cloud-base  $N_{d90}$  mostly larger than the ship measured CCN.

The result here is contrary to previous studies of the same methodology (Rosenfeld et al. 2016), that included tropical and midlatitude terrestrial locations and some oceanic trade wind cumulus. The satellite-retrieved  $N_{d90}$  showed good agreement with the surface measured CCN, probably due to the strong coupling of these convective clouds with the surface. The fundamental difference is that the clouds in the Southern Oceans were mostly stratocumulus and stratus, which are often decoupled from the ocean surface.

Therefore, an obvious next step in the research is analyzing the relationships between the satellite-retrieved and ship-measured CCN based on the coupling state of the clouds.

**COMPARISON OF MODEL AND MEASUREMENT RESULTS.** On average, the GLOMAP model underestimates  $\text{CCN}_{0.2}$  number concentrations by roughly 50% in 80% of the grid boxes covering the ship track (Fig. 9). The regions of highest underestimation are close to the coast of Antarctica during leg 2, close to South Africa and around 45°E during leg 1. These regions coincide with the highest concentrations of gaseous MSA (for leg 1 this remains speculation since we do not have measurements but it is backed up by particulate MSA observations). This preliminary model–measurement comparison suggests that the model may be missing an important

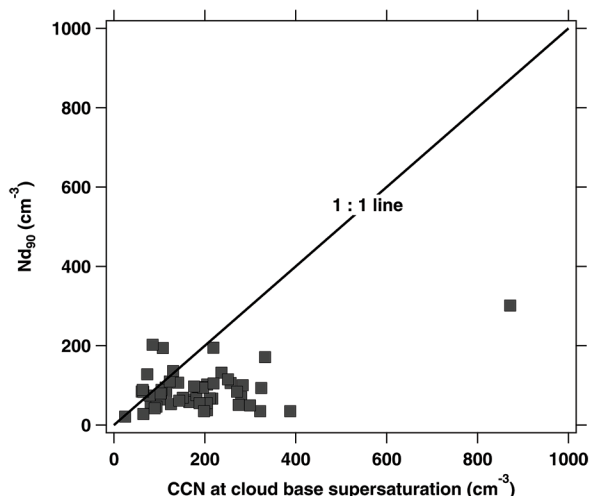


**FIG. 8.** Satellite-retrieved cloud droplet concentrations  $N_{d90}$  vs ship-measured CCN number concentrations interpolated to the same cloud-base supersaturation for clouds with a geometrical depth of up to 800 m and within 150 km of the ship.

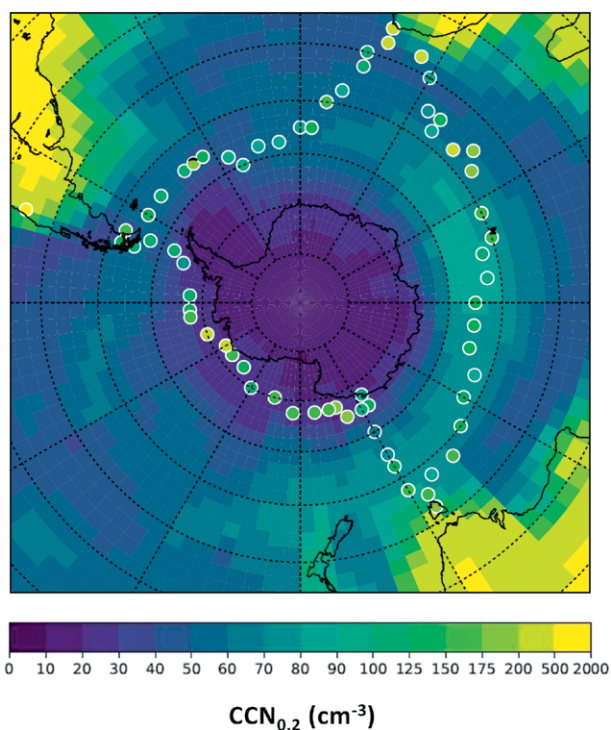


**FIG. 9.** Comparison of the global aerosol model GLOMAP simulation of monthly mean  $\text{CCN}_{0.2}$  with ACE-SPACE in situ measurements.

source of high-latitude CCN. Another possibility is that the degree of cloud processing in the model may be too low in these regions, since our analysis indicates that repeated cloud processing increases the particle number concentration in the CCN size range.

Modeled  $\text{CCN}_{0.2}$  concentrations are also underestimated by at least 10% in places where MSA concentrations are low. There are multiple parameters in the model that could cause this underestimation. For example, sea spray and DMS emission fluxes from the ocean surface layer may be too low in the model. Alternatively, a dry deposition that is too vigorous could remove aerosols too quickly from the atmosphere. Aerosol removal through excessive precipitation could also cause the  $\text{CCN}_{0.2}$  bias, and several parameters affect aerosol size distributions, cloud droplet activation and aerosol removal rates by precipitation.

In this analysis we compared the model mean output (from a sample of 1 million model variants; Johnson et al. 2018) with measured values. The degree to which individual model variants and their associated parameter values agree with measurements will be evaluated in a future study. A thorough model–observation comparison requires rigorous statistical techniques that account for multiple sources of uncertainty such as observation representativeness errors (Schutgens et al. 2017), which are beyond the scope of this article.

**SUMMARY AND OUTLOOK.** The first results from ACE-SPACE highlight that the Southern Ocean is a region with highly heterogeneous aerosol properties. The areas around the strong westerly wind belt are characterized by significant sea spray contributions to the total particle and CCN number concentrations in the MBL. Future work will link detailed wave and wind observations to sea spray production.

In the Ross and Amundsen Sea polynyas (leg 2), biogenic emissions appear to play an important role for CCN abundance. There are a number of open questions associated with this observation. First, even though this particular region was probed during a phytoplankton bloom period, it was not the only region with microbial activity but showed the clearest link to high CCN concentrations. Hence, either DMS production from dimethylsulfoniopropionate in the water and/or DMS fluxes into the atmosphere were enhanced. Second, the major pathway of how MSA is added to the particle phase remains to be identified. There are two possibilities: it can condense from the gas into the particle phase, or it can be added during cloud processing. The latter process would be consistent with the reduced efficiency of wet removal because of droplet evaporation or snowflake sublimation in the cold and dry airmasses from Antarctica.

Our results also indicate that the absence of MSA-related processes in the aerosol model could

explain the underestimation of CCN concentration, particularly in high aerosol-MSA regions. Given that the number of CCN influence  $N_p$ , this is an important issue to solve, especially close to the coast of Antarctica where clouds could impact the surface snow mass balance by influencing both the surface energy budget and precipitation. Further studies are planned that more closely investigate the linkages between CCN number concentrations and model simulations that take DMS emissions fluxes and particle phase MSA into account.

A comparison of satellite-retrieved  $N_{d90}$  and ship-based measurements of CCN shows a clear underestimation of CCN from remote sensing, even for coupled cloud cases. This is a strong indication of the importance of surface sources as opposed to the free troposphere for particle origin. Further investigation is underway to understand the cause of the discrepancy between the remote sensing and in situ measurements.

We did not find direct evidence for new particle formation as an important source of CCN. However, some nucleation events were observed and a nucleation mode was present in the clustered particle size distributions. A dedicated study will investigate the gases involved in these events and the fate of the nucleation mode in the atmosphere.

Our ice nucleating particle findings suggest that concentrations are lower than in Northern Hemisphere marine airmasses and that concentrations decreased from summer toward fall with only small differences between open-ocean and coastal Antarctic samples. The ACE-SPACE INP concentrations are also consistent with findings of a recent study in the Southern Ocean (McCluskey et al. 2018a), but much lower than results from several decades ago (Bigg 1973). More detailed studies including information on potential island effects, long-range transport and fluorescent and microbial particles are underway.

The ACE-SPACE project is motivated by the idea of constraining uncertainty in anthropogenic radiative forcing from aerosol–cloud interactions through measurement of preindustrial-like aerosol–cloud interactions. We have shown that the in situ data are suitable for constraining the aerosol model for preindustrial-like conditions. After a detailed model–measurement comparison, we will use the aerosol model to further constrain uncertainties of global radiative forcing from aerosol–cloud interactions.

**ACKNOWLEDGMENTS.** ACE-SPACE, JS, IT, AT, SH, and MD received funding from EPFL, the Swiss Polar Institute, and Ferring Pharmaceuticals. ACE-SPACE was

carried out with additional support from the European FP7 project BACCHUS (Grant Agreement 49603445). SL received funding from the Swiss Data Science Center project c17-02. AB received funding from the Swiss National Science Foundation (Grant 200021\_169090). FT was supported by the Swiss National Science Foundation (Grant 20F121\_138017). The U.K. Natural Environment Research Council sponsored the iDirac development (NE/K016377/1) and the Doctoral Training Partnership for CB. CT received funding from DFG within the SPP 1158 (Grant STR 453/12-1). KC is currently a Royal Society Wolfson Merit Award holder. LR, JSJ, and KC acknowledge funding from NERC under Grants AEROS, ACID-PRUF, GASSP, and A-CURE (NE/G006172/1, NE/I020059/1, NE/J024252/1, and NE/P013406/1), and were also supported by the U.K.–China Research and Innovation Partnership Fund through the Met Office Climate Science for Service Partnership China as part of the Newton Fund. This work used the ARCHER U.K. National Supercomputing Service, [www.archer.ac.uk](http://www.archer.ac.uk) and JASMIN super-data-cluster (<https://doi.org/10.1109/BigData.2013.6691556>), via the Center for Environmental Data Analysis. ARCHER project allocation n02-FREPPPE and the Leadership Project allocation n02-CCPPE were used to create the perturbed parameter ensemble. KL was funded by the European Commission's Horizon 2020 programme (MSCA-IF project Nano-CAVa, 656994). MG received funding from the ERC under Grant ERC-CoG-615922-BLACARAT. We thank MeteoSwiss for providing access to operational ECMWF data.

## APPENDIX A: IN SITU MEASUREMENTS.

The two air-sampling inlets were built after the Global Atmosphere Watch recommendations and as operated on the Jungfrauoch, Switzerland (Weingartner et al. 1999). They sample particles up to 40  $\mu\text{m}$  in diameter under wind conditions of up to 20  $\text{m s}^{-1}$ . Particle number concentrations were obtained from CPCs with different lower cutoff diameters: TSI 3022, 7 nm; TSI 3772, 10 nm; TSI 3010D, 20 nm. The NAIS instrument was used to measure particle number size distributions from 2 to 40 nm. A home-built SMPS (Wiedensohler et al. 2012) sized particles between 11 and 400 nm, an APS 3321 between 500 nm and 19  $\mu\text{m}$ , and a WIBS-4 between 0.5 and 12.5  $\mu\text{m}$ . All sizes are given as diameters. The WIBS determines also the number and size of fluorescent particles, and the NAIS determines in addition the ion size distribution between 0.8 and 40 nm and was used in conjunction with the atmospheric pressure interface time-of-flight mass spectrometer (APi-TOF; Junninen et al. 2010) capable of measuring the atmospheric ion composition or the composition of neutral clusters when using an upstream chemical ionization unit (CI-APi-TOF, nitrate-based in our case).

Note that data are preliminary, and updated versions can be found on <https://zenodo.org/communities/spi-ace> as soon as available. The bulk chemical composition of the submicron aerosol was determined with a time-of-flight aerosol chemical speciation monitor (ACSM; Ng et al. 2011; Fröhlich et al. 2013), which quantifies the mass concentration of nonrefractory aerosol (defined as evaporating at 600°C), meaning that relative variations of sea salt concentrations can be determined but not well quantified. The major ion composition of particulate matter with a diameter <10  $\mu\text{m}$  ( $\text{PM}_{10}$ ) is based on ion chromatography from 24-h filters. The CCN number concentration was measured by a CCNC (Roberts and Nenes 2005), while the INP concentrations were determined based on 8-h filters processed with the droplet freezing array INDA (Ice Nucleation Droplet Array) after Conen et al. (2012) and Budke and Koop (2015). Trace gases ( $\text{O}_3$ ,  $\text{CH}_4$ ,  $\text{CO}$ ,  $\text{CO}_2$ ) were measured with a PICARRO G2401 to identify different types of airmasses as well as marine biogenic emissions. Atmospheric isoprene concentrations were determined by the custom-built portable gas chromatograph iDirac (Visakorpi et al. 2018). Equivalent black carbon, trace gases data such as  $\text{CO}$  and  $\text{CO}_2$ , and the 10-s variability of particle number concentrations were used to identify the influence of ship exhaust. Identified exhaust periods are not included here and constitute about 50% of the total data. Size-dependent particle losses in the inlet lines were determined experimentally after the cruise and data are corrected accordingly. Losses were <10% for submicron particles and about 15% for supermicron particles.

The cloud base was measured by a Vaisala Ceilometer CL31 that was part of the automated ship-based weather station.

**APPENDIX B: REMOTE SENSING.** We obtained cloud droplet number concentrations from MODIS products (Szczo drak et al. 2001) and cloud-base updraft. The methodology of Zhu et al. (2018) was used to maximize the relationships between  $N_d$  and CCN. The retrieval was focused on the brightest 10% of the clouds in the area of interest, in which the clouds were closest to adiabatic, as assumed in the  $N_d$  retrieval algorithm. The cloud-base updraft was obtained from the cloud-top radiative cooling rate, which was shown by Zheng et al. (2016) to be linearly related to cloud-base updraft. The cloud-base maximum supersaturation  $S$  was calculated by

$$S = C(T_b, P_b)W_b^{3/4}N_d^{-1/2},$$

where  $C$  is a coefficient that is based on cloud-base temperature  $T_b$ , cloud-base updraft  $W_b$ , and pressure

$P_b$  (Pinsky et al. 2012). By definition,  $N_d$  is the then number of CCN at supersaturation  $S$ .

**APPENDIX C: MODELING.** *Back trajectory modeling.* Ten-day air parcel backward trajectories were calculated with the Lagrangian analysis tool LAGRANTO (Wernli and Davies 1997; Sprenger and Wernli 2015) using the three-dimensional wind fields from the 3-hourly global operational analysis data of the European Centre for Medium-Range Weather Forecasts (ECMWF). The ECMWF analysis fields were interpolated on a regular horizontal grid of  $0.5^\circ$  horizontal resolution on each of the 137 vertical model levels. In total 56 trajectories were launched every hour from the surface to 500 hPa in steps of 10 hPa with a higher resolution of 1–5 hPa in the lowermost 20 hPa. Additionally, the sea surface temperature (SST) from ECMWF operational analyses was interpolated along the track, and compared to the measured in situ air temperature  $T_a$ . If  $SST > T_a$ , we classified the local airmass as being part of the cold sector of a frontal system, and if  $SST < T_a$  as part of the warm sector.

For the intercomparison of measured wind speed and ECMWF operational output that provides wind speed at 10-m neutral stability we converted it to friction velocity with the wind-speed-dependent drag coefficient from the COARE 3.5 bulk flux model (Edson et al. 2013). The ERA-Interim output of surface sensible and latent heat flux were used together with the friction velocity to estimate the Monin–Obukhov length scale, which was used with the stability functions provided in Fairall et al. (2003) to relate the ERA-Interim 10-m wind speed to the measured 30-m wind speed. According to Schmidt et al. (2017), ERA-Interim, the reanalysis product based on ECMWF, is the most accurate product to represent temporal variability of winds.

*Modeling with GLOMAP.* The GLOMAP-mode model, used in the UKCA, simulates new particle formation, aerosol coagulation, gas-to-particle transfer, cloud processing of aerosols, and both dry and wet deposition of gases and aerosols. In our model setup,  $2.5^\circ$  latitude  $\times$   $3.75^\circ$  longitude, GLOMAP resolves five aerosol components—sulfate, organic carbon, black carbon, sea salt, and dust—into seven modes: soluble modes in nucleation, Aitken, accumulation, and coarse size ranges and insoluble modes in all but the nucleation size range. Within each particle size mode, chemical components are assumed to be internally mixed and particles follow the lognormal number–size distribution. Particles form through binary homogeneous nucleation (Vehkamäki et al. 2002) throughout the

atmosphere and through organically mediated nucleation (Metzger et al. 2010) in the planetary boundary layer. Particles grow following microphysical processes such as condensation of gas species and coagulation between particles. They are moved from one mode to another when the mean modal size becomes larger than a prescribed threshold, or when insoluble particles are aged to become soluble. Aerosols are removed from the atmosphere through gravitational settling, turbulent mixing, nucleation into cloud drops (followed by autoconversion to rain), and impact by precipitating rain drops (Kipling et al. 2013).

Soluble particles grow according to the relative atmospheric humidity using composition-dependent hygroscopicity factors ( $\kappa$ ; kappa) in accordance with the Köhler theory. The activation of aerosols into cloud droplets is calculated using distributions of subgrid vertical velocities (West et al. 2014) and the removal of cloud droplets is calculated by the host model. The SOCRATES radiation code (Edwards and Slingo 1996) is used within HadGEM3-UKCA to calculate the radiative effects of aerosols.

Sea spray aerosols are emitted into the atmosphere using the Gong (2003) surface-wind-speed-dependent parameterization. Surface ocean dimethylsulfide concentrations are prescribed using the Kettle and Andreae (2000) dataset and are emitted into the atmosphere using a surface-wind-speed-dependent parameterization (Nightingale et al. 2000). Primary marine organic aerosols are not explicitly in our simulations.

Horizontal winds above around 2 km were nudged toward ERA-Interim for the year 2006 in the model, not the year measurements were collected. Therefore, simulated and measured wind speeds are only weakly correlated ( $R^2 = 0.13$ ). However, simulated  $CCN_{0.2}$  concentrations and wind speeds are uncorrelated over the locations where measurements were collected. Wind speeds have compensating effects on aerosol and CCN concentrations (Korhonen et al. 2010). Higher wind speeds increase the emission flux of sea spray aerosols and aerosol precursors (DMS), but are also associated with larger waves that increase the removal rate of near-surface aerosols, at least on the scales simulated by global climate models. The lack of CCN dependence on 10-m wind speeds suggests our model–measurement comparison results will not be affected by the meteorological year used in the model.

## REFERENCES

- Albrecht, B. A., 1989: Aerosols, cloud microphysics, and fractional cloudiness. *Science*, **245**, 1227–1230, <https://doi.org/10.1126/science.245.4923.1227>.

- Asmi, E., and Coauthors, 2010: Hygroscopicity and chemical composition of Antarctic sub-micrometre aerosol particles and observations of new particle formation. *Atmos. Chem. Phys.*, **10**, 4253–4271, <https://doi.org/10.5194/acp-10-4253-2010>.
- Ayers, G. P., J. M. Caine, R. W. Gillett, and J. P. Ivey, 1997: Atmospheric sulphur and cloud condensation nuclei in marine air in the Southern Hemisphere. *Philos. Trans. Roy. Soc. London*, **352B**, 203–211, <https://doi.org/10.1098/rstb.1997.0015>.
- Bates, T. S., and P. K. Quinn, 1997: Dimethylsulfide (DMS) in the equatorial Pacific Ocean (1982 to 1996): Evidence of a climate feedback? *Geophys. Res. Lett.*, **24**, 861–864, <https://doi.org/10.1029/97GL00784>.
- , B. J. Huebert, J. L. Gras, F. B. Griffiths, and P. A. Durkee, 1998: International Global Atmospheric Chemistry (IGAC) Project's First Aerosol Characterization Experiment (ACE 1): Overview. *J. Geophys. Res.*, **103**, 16 297–16 318, <https://doi.org/10.1029/97JD03741>.
- Bigg, E. K., 1973: Ice nucleus concentrations in remote areas. *J. Atmos. Sci.*, **30**, 1153–1157, [https://doi.org/10.1175/1520-0469\(1973\)030<1153:INCIRA>2.0.CO;2](https://doi.org/10.1175/1520-0469(1973)030<1153:INCIRA>2.0.CO;2).
- Bodas-Salcedo, A., and Coauthors, 2014: Origins of the solar radiation biases over the Southern Ocean in CFMIP2 models. *J. Climate*, **27**, 41–56, <https://doi.org/10.1175/JCLI-D-13-00169.1>.
- Boers, R., J. B. Jensen, P. B. Krummel, and H. Gerber, 1996: Microphysical and short-wave radiative structure of wintertime stratocumulus clouds over the Southern Ocean. *Quart. J. Roy. Meteor. Soc.*, **122**, 1307–1339, <https://doi.org/10.1002/qj.49712253405>.
- , —, and —, 1998: Microphysical and short-wave radiative structure of stratocumulus clouds over the Southern Ocean: Summer results and seasonal differences. *Quart. J. Roy. Meteor. Soc.*, **124**, 151–168, <https://doi.org/10.1002/qj.49712454507>.
- Bony, S., and B. Stevens, 2012: Clouds, circulation and climate sensitivity: How the interactions between clouds, greenhouse gases and aerosols affect temperature and precipitation in a changing climate. WCRP Grand Challenge White Paper, 7 pp., [www.wcrp-climate.org/images/documents/grand\\_challenges/GC4\\_Clouds\\_14nov2012.pdf](http://www.wcrp-climate.org/images/documents/grand_challenges/GC4_Clouds_14nov2012.pdf).
- Budke, C., and T. Koop, 2015: BINARY: An optical freezing array for assessing temperature and time dependence of heterogeneous ice nucleation. *Atmos. Meas. Tech.*, **8**, 689–703, <https://doi.org/10.5194/amt-8-689-2015>.
- Carlsaw, K., and Coauthors, 2013: Large contribution of natural aerosols to uncertainty in indirect forcing. *Nature*, **503**, 67–71, <https://doi.org/10.1038/nature12674>.
- Ceppi, P., Y.-T. Hwang, D. M. W. Frierson, and D. L. Hartmann, 2012: Southern Hemisphere jet latitude biases in CMIP5 models linked to shortwave cloud forcing. *Geophys. Res. Lett.*, **39**, L19708, <https://doi.org/10.1029/2012GL053115>.
- Chen, Q., T. Sherwen, M. Evans, and B. Alexander, 2018: DMS oxidation and sulfur aerosol formation in the marine troposphere: A focus on reactive halogen and multiphase chemistry. *Atmos. Chem. Phys.*, **18**, 13 617–13 637, <https://doi.org/10.5194/acp-18-13617-2018>.
- Clarke, A. D., J. L. Varner, F. Eisele, R. L. Mauldin, D. Tanner, and M. Litchy, 1998: Particle production in the remote marine atmosphere: Cloud outflow and subsidence during ACE 1. *J. Geophys. Res.: Atmos.*, **103**, 16 397–16 409, <https://doi.org/10.1029/97JD02987>.
- Conen, F., S. Henne, C. E. Morris, and C. Alewell, 2012: Atmospheric ice nucleators active  $\geq -12$  °C may be quantified on PM10 filters. *Atmos. Meas. Tech.*, **5**, 321–327, <https://doi.org/10.5194/amt-5-321-2012>.
- Cozic, J., B. Verheggen, S. Mertes, P. Connolly, K. Bower, A. Petzold, U. Baltensperger, and E. Weingartner, 2007: Scavenging of black carbon in mixed phase clouds at the high alpine site Jungfraujoch. *Atmos. Chem. Phys.*, **7**, 1797–1807, <https://doi.org/10.5194/acp-7-1797-2007>.
- Dall'Osto, M., and Coauthors, 2017: Antarctic sea ice region as a source of biogenic organic nitrogen in aerosols. *Sci. Rep.*, **7**, 6047, <https://doi.org/10.1038/s41598-017-06188-x>.
- Dee, D. P., and Coauthors, 2011: The ERA-Interim reanalysis: Configuration and performance of the data assimilation system. *Quart. J. Roy. Meteor. Soc.*, **137**, 553–597, <https://doi.org/10.1002/qj.828>.
- Edson, J. B., and Coauthors, 2013: On the exchange of momentum over the open ocean. *J. Phys. Oceanogr.*, **43**, 1589–1610, <https://doi.org/10.1175/JPO-D-12-0173.1>.
- Edwards, J. M., and A. Slingo, 1996: Studies with a flexible new radiation code. I: Choosing a configuration for a large-scale model. *Quart. J. Roy. Meteor. Soc.*, **122**, 689–719, <https://doi.org/10.1002/qj.49712253107>.
- Fairall, C. W., E. F. Bradley, J. E. Hare, A. A. Grachev, and J. B. Edson, 2003: Bulk parameterization of air–sea fluxes: Updates and verification for the COARE algorithm. *J. Climate*, **16**, 571–591, [https://doi.org/10.1175/1520-0442\(2003\)016<0571:BPOASF>2.0.CO;2](https://doi.org/10.1175/1520-0442(2003)016<0571:BPOASF>2.0.CO;2).
- Flato, G., and Coauthors, 2013: Evaluation of climate models. *Climate Change 2013: The Physical Science Basis*, T. F. Stocker et al., Eds., Cambridge University Press, 741–866.
- Fossum, K. N., and Coauthors, 2018: Summertime primary and secondary contributions to Southern

- Ocean cloud condensation nuclei. *Sci. Rep.*, **8**, 13844, <https://doi.org/10.1038/s41598-018-32047-4>.
- Freud, E. and D. Rosenfeld, 2012: Linear relation between convective cloud drop number concentration and depth for rain initiation. *J. Geophys. Res.: Atmos.*, **117**, D02207, <https://doi.org/10.1029/2011JD016457>.
- Fröhlich, R., and Coauthors, 2013: The ToF-ACSM: A portable aerosol chemical speciation monitor with TOFMS detection. *Atmos. Meas. Tech.*, **6**, 3225–3241, <https://doi.org/10.5194/amt-6-3225-2013>.
- Gong, S. L., 2003: A parameterization of sea-salt aerosol source function for sub- and super-micron particles. *Global Biogeochem. Cycles*, **17**, 1097, <https://doi.org/10.1029/2003GB002079>.
- Goren, T., and D. Rosenfeld, 2012: Satellite observations of ship emission induced transitions from broken to closed cell marine stratocumulus over large areas. *J. Geophys. Res.: Atmos.*, **117**, <https://doi.org/10.1029/2012JD017981>.
- Gras, J. L., S. I. Jimi, S. T. Siems, and P. B. Krummel, 2009: Postfrontal nanoparticles at Cape Grim: Observations. *Environ. Chem.*, **6**, 508–514, <https://doi.org/10.1071/EN09075>.
- Grazioli, J., J.-B. Madeleine, H. Gallée, R. M. Forbes, C. Genthon, G. Krinner, and A. Berne, 2017: Katabatic winds diminish precipitation contribution to the Antarctic ice mass balance. *Proc. Natl. Acad. Sci. USA*, **114**, 102858–102863, <https://doi.org/10.1073/pnas.1707633114>.
- Hamilton, D. S., L. A. Lee, K. J. Pringle, C. L. Reddington, D. V. Spracklen, and K. S. Carslaw, 2014: Occurrence of pristine aerosol environments on a polluted planet. *Proc. Natl. Acad. Sci. USA*, **111**, 18466–18471, <https://doi.org/10.1073/pnas.1415440111>.
- Hanley, K. E., S. E. Belcher, and P. P. Sullivan, 2010: A global climatology of wind–wave interaction. *J. Phys. Oceanogr.*, **40**, 1263–1282, <https://doi.org/10.1175/2010JPO4377.1>.
- Hodshire, A. L., P. Campuzano-Jost, J. K. Kodros, B. Croft, B. A. Nault, J. C. Schroder, J. L. Jimenez, and J. R. Pierce, 2019: The potential role of methanesulfonic acid (MSA) in aerosol formation and growth and the associated radiative forcings. *Atmos. Chem. Phys.*, **19**, 3137–3160, <https://doi.org/10.5194/acp-19-3137-2019>.
- Hoppel, W. A., and G. M. Frick, 1990: Submicron aerosol size distributions measured over the tropical and South Pacific. *Atmos. Environ.*, **24A**, 645–659, [https://doi.org/10.1016/0960-1686\(90\)90020-N](https://doi.org/10.1016/0960-1686(90)90020-N).
- Huang, Y., C. N. Franklin, S. T. Siems, M. J. Manton, T. Chubb, A. Lock, S. Alexander, and A. Klekociuk, 2015: Evaluation of boundary-layer cloud forecasts over the Southern Ocean in a limited-area numerical weather prediction system using in situ, spaceborne and ground-based observations. *Quart. J. Roy. Meteor. Soc.*, **141**, 2259–2276, <https://doi.org/10.1002/qj.2519>.
- Humphries, R. S., and Coauthors, 2015: Boundary layer new particle formation over East Antarctic sea ice – Possible Hg-driven nucleation? *Atmos. Chem. Phys.*, **15**, 132339–132364, <https://doi.org/10.5194/acp-15-13339-2015>.
- , A. R. Klekociuk, R. Schofield, M. Keywood, J. Ward, and S. R. Wilson, 2016: Unexpectedly high ultrafine aerosol concentrations above East Antarctic sea-ice. *Atmos. Chem. Phys.*, **16**, 2185–2206, <https://doi.org/10.5194/acp-16-2185-2016>.
- Hwang, Y.-T., and D. M. W. Frierson, 2013: Link between the double-Intertropical Convergence Zone problem and cloud biases over the Southern Ocean. *Proc. Natl. Acad. Sci. USA*, **110**, 4935–4940, <https://doi.org/10.1073/pnas.1213302110>.
- Johnson, G. R., Z. Ristovski, and L. Morawska, 2004: Method for measuring the hygroscopic behaviour of lower volatility fractions in an internally mixed aerosol. *J. Aerosol Sci.*, **35**, 443–455, <https://doi.org/10.1016/j.jaerosci.2003.10.008>.
- Johnson, J. S., and Coauthors, 2018: The importance of comprehensive parameter sampling and multiple observations for robust constraint of aerosol radiative forcing. *Atmos. Chem. Phys.*, **18**, 13 031–13 053, <https://doi.org/10.5194/acp-18-13031-2018>.
- Johnson, R., P. G. Strutton, S. W. Wright, A. McMinn, and K. M. Meiners, 2013: Three improved satellite chlorophyll algorithms for the Southern Ocean. *J. Geophys. Res. Oceans*, **118**, 3694–3703, <https://doi.org/10.1002/jgrc.20270>.
- Jokinen, T., and Coauthors, 2018: Ion-induced sulfuric acid–ammonia nucleation drives particle formation in coastal Antarctica. *Sci. Adv.*, **4**, eaat9744, <https://doi.org/10.1126/sciadv.aat9744>.
- Junninen, H., and Coauthors, 2010: A high-resolution mass spectrometer to measure atmospheric ion composition. *Atmos. Meas. Tech.*, **3**, 1039–1053, <https://doi.org/10.5194/amt-3-1039-2010>.
- Kay, J. E., C. Wall, V. Yettella, B. Medeiros, C. Hannay, P. Caldwell, and C. Bitz, 2016: Global climate impacts of fixing the Southern Ocean shortwave radiation bias in the Community Earth System Model (CESM). *J. Climate*, **29**, 4617–4636, <https://doi.org/10.1175/JCLI-D-15-0358.1>.
- Kettle, A. J., and M. O. Andreae, 2000: Flux of dimethylsulfide from the oceans: A comparison of updated data sets and flux models. *J. Geophys. Res.*, **105**, 26 793–26 808, <https://doi.org/10.1029/2000JD900252>.
- Kipling, Z., P. Stier, J. P. Schwarz, A. E. Perring, J. R. Spackman, G. W. Mann, C. E. Johnson, and P. J.

- Telford, 2013: Constraints on aerosol processes in climate models from vertically-resolved aircraft observations of black carbon. *Atmos. Chem. Phys.*, **13**, 5969–5986, <https://doi.org/10.5194/acp-13-5969-2013>.
- Kohout, A. L., M. J. M. Williams, S. M. Dean, and M. H. Meylan, 2014: Storm-induced sea-ice breakup and the implications for ice extent. *Nature*, **509**, 604–607, <https://doi.org/10.1038/nature13262>.
- Korhonen, H., K. S. Carslaw, D. V. Spracklen, G. W. Mann, and M. T. Woodhouse, 2008: Influence of oceanic dimethyl sulfide emissions on cloud condensation nuclei concentrations and seasonality over the remote Southern Hemisphere oceans: A global model study. *J. Geophys. Res.*, **113**, D15204, <https://doi.org/10.1029/2007JD009718>.
- , —, P. M. Forster, S. Mikkonen, N. D. Gordon, and H. Kokkola, 2010: Aerosol climate feedback due to decadal increases in Southern Hemisphere wind speeds. *Geophys. Res. Lett.*, **37**, L02805, <https://doi.org/10.1029/2009GL041320>.
- Law, C. S., and Coauthors, 2017: Overview and preliminary results of the Surface Ocean Aerosol Production (SOAP) campaign. *Atmos. Chem. Phys.*, **17**, 13 645–13 667, <https://doi.org/10.5194/acp-17-13645-2017>.
- Mace, G. G., and A. Protat, 2018: Clouds over the Southern Ocean as observed from the R/V *Investigator* during CAPRICORN. Part I: Cloud occurrence and phase partitioning. *J. Appl. Meteor. Climatol.*, **57**, 1783–1803, <https://doi.org/10.1175/JAMC-D-17-0194.1>.
- Mann, G. W., K. S. Carslaw, D. V. Spracklen, D. A. Ridley, P. T. Manktelow, M. P. Chipperfield, S. J. Pickering, and C. E. Johnson, 2010: Description and evaluation of GLOMAP-mode: A modal global aerosol microphysics model for the UKCA composition-climate model. *Geosci. Model Dev.*, **3**, 519–551, <https://doi.org/10.5194/gmd-3-519-2010>.
- McCluskey, C. S., and Coauthors, 2018a: Observations of ice nucleating particles over Southern Ocean waters. *Geophys. Res. Lett.*, **45**, 11 989–11 997, <https://doi.org/10.1029/2018GL079981>.
- , and Coauthors, 2018b: Marine and terrestrial organic ice-nucleating particles in pristine marine to continentally influenced Northeast Atlantic air masses. *J. Geophys. Res. Atmos.*, **123**, 6196–6212, <https://doi.org/10.1029/2017JD028033>.
- McCoy, D. T., and Coauthors, 2015: Natural aerosols explain seasonal and spatial patterns of Southern Ocean cloud albedo. *Sci. Adv.*, **1**, e1500157, <https://doi.org/10.1126/sciadv.1500157>.
- Metzger, A., and Coauthors, 2010: Evidence for the role of organics in aerosol particle formation under atmospheric conditions. *Proc. Natl. Acad. Sci. USA*, **107**, 6646–6651, <https://doi.org/10.1073/pnas.0911330107>.
- Modini, R. L., and Coauthors, 2015: Primary marine aerosol-cloud interactions off the coast of California. *J. Geophys. Res. Atmos.*, **120**, 4282–4303, <https://doi.org/10.1002/2014JD022963>.
- Monahan, E. C., D. E. Spiel, and K. L. Davidson, 1986: A model of marine aerosol generation via whitecaps and wave disruption. *Oceanic Whitecaps and Their Role in Air-Sea Exchange Processes*, E. C. Monahan and G. M. Niocaill, Eds., Springer, 167–174, [https://doi.org/10.1007/978-94-009-4668-2\\_16](https://doi.org/10.1007/978-94-009-4668-2_16).
- Ng, N. L., and Coauthors, 2011: An Aerosol Chemical Speciation Monitor (ACSM) for routine monitoring of the composition and mass concentrations of ambient aerosol. *Aerosol Sci. Technol.*, **45**, 780–794, <https://doi.org/10.1080/02786826.2011.560211>.
- Nightingale, P. D., P. S. Liss, and P. Schlosser, 2000: Measurements of air-sea gas transfer during an open ocean algal bloom. *Geophys. Res. Lett.*, **27**, 2117–2120, <https://doi.org/10.1029/2000GL011541>.
- O'Connor, F. M., and Coauthors, 2014: Evaluation of the new UKCA climate-composition model – Part 2: The Troposphere. *Geosci. Model Dev.*, **7**, 41–91, <https://doi.org/10.5194/gmd-7-41-2014>.
- O'Dowd, C. D., J. A. Lowe, M. H. Smith, B. Davison, C. N. Hewitt, and R. M. Harrison, 1997: Biogenic sulphur emissions and inferred non-sea-salt-sulphate cloud condensation nuclei in and around Antarctica. *J. Geophys. Res.*, **102**, 12 839–12 854, <https://doi.org/10.1029/96JD02749>.
- , and Coauthors, 2004: Biogenically driven organic contribution to marine aerosol. *Nature*, **431**, 676–680, <https://doi.org/10.1038/nature02959>.
- O'Shea, S. J., and Coauthors, 2017: In situ measurements of cloud microphysics and aerosol over coastal Antarctica during the MAC campaign. *Atmos. Chem. Phys.*, **17**, 13 049–13 070, <https://doi.org/10.5194/acp-17-13049-2017>.
- Ovadnevaite, J., and Coauthors, 2017: Surface tension prevails over solute effect in organic-influenced cloud droplet activation. *Nature*, **546**, 637–641, <https://doi.org/10.1038/nature22806>.
- Papritz, L., S. Pfahl, I. Rudeva, I. Simmonds, H. Sodemann, and H. Wernli, 2014: The role of extratropical cyclones and fronts for Southern Ocean freshwater fluxes. *J. Climate*, **27**, 6205–6224, <https://doi.org/10.1175/JCLI-D-13-00409.1>.
- Peters, M. D., and S. M. Kreidenweis, 2007: A single parameter representation of hygroscopic growth and cloud condensation nucleus activity. *Atmos. Chem. Phys.*, **7**, 1961–1971, <https://doi.org/10.5194/acp-7-1961-2007>.

- Pikridas, M., and Coauthors, 2015: In situ formation and spatial variability of particle number concentration in a European megacity. *Atmos. Chem. Phys.*, **15**, 10219–10237, <https://doi.org/10.5194/acp-15-10219-2015>.
- Pinsky, M., A. Khain, I. Mazin, and A. Korolev, 2012: Analytical estimation of droplet concentration at cloud base. *J. Geophys. Res.*, **117**, D18211, <https://doi.org/10.1029/2012JD017753>.
- Prather, K. A., and Coauthors, 2013: Bringing the ocean into the laboratory to probe the chemical complexity of sea spray aerosol. *Proc. Natl. Acad. Sci. USA*, **110**, 7550–7555, <https://doi.org/10.1073/pnas.1300262110>.
- Protat, A., E. Schulz, L. Rikus, Z. Sun, Y. Xiao, and M. Keywood, 2017: Shipborne observations of the radiative effect of Southern Ocean clouds. *J. Geophys. Res. Atmos.*, **122**, 318–328, <https://doi.org/10.1002/2016JD026061>.
- Quinn, P. K., T. S. Bates, K. S. Schulz, D. J. Coffman, A. A. Frossard, L. M. Russell, W. C. Keene, and D. J. Kieber, 2014: Contribution of sea surface carbon pool to organic matter enrichment in sea spray aerosol. *Nat. Geosci.*, **7**, 228–232, <https://doi.org/10.1038/ngeo2092>.
- , D. J. Coffman, J. E. Johnson, L. M. Upchurch, and T. S. Bates, 2017: Small fraction of marine cloud condensation nuclei made up of sea spray aerosol. *Nat. Geosci.*, **10**, 674–679, <https://doi.org/10.1038/ngeo3003>.
- Regayre, L. A., and Coauthors, 2014: Uncertainty in the magnitude of aerosol-cloud radiative forcing over recent decades. *Geophys. Res. Lett.*, **41**, 9040–9049, <https://doi.org/10.1002/2014GL062029>.
- , and Coauthors, 2018: Aerosol and physical atmosphere model parameters are both important sources of uncertainty in aerosol ERF. *Atmos. Chem. Phys.*, **18**, 9975–10006, <https://doi.org/10.5194/acp-18-9975-2018>.
- Reutter, P., and Coauthors, 2009: Aerosol- and updraft-limited regimes of cloud droplet formation: Influence of particle number, size and hygroscopicity on the activation of cloud condensation nuclei (CCN). *Atmos. Chem. Phys.*, **9**, 7067–7080, <https://doi.org/10.5194/acp-9-7067-2009>.
- Roberts, G. C., and A. Nenes, 2005: A continuous-flow streamwise thermal-gradient CCN chamber for atmospheric measurements. *Aerosol Sci. Technol.*, **39**, 206–221, <https://doi.org/10.1080/027868290913988>.
- Rosenfeld, D., Y. J. Kaufman, and I. Koren, 2006: Switching cloud cover and dynamical regimes from open to closed Benard cells in response to the suppression of precipitation by aerosols. *Atmos. Chem. Phys.*, **6**, 2503–2511, <https://doi.org/10.5194/acp-6-2503-2006>.
- Rosenfeld, D., and Coauthors, 2016: Satellite retrieval of cloud condensation nuclei concentrations by using clouds as CCN chambers. *Proc. Natl. Acad. Sci. USA*, **113**, 5828–5834, <https://doi.org/10.1073/pnas.1514044113>.
- , Y. Zhu, M. Wang, Y. Zheng, T. Goren, and S. Yu, 2019: Aerosol-driven droplet concentrations dominate coverage and water of oceanic low level clouds. *Science*, **363**, eaav0566, <https://doi.org/10.1126/science.aav0566>.
- Saxena, V. K., 1996: Bursts of cloud condensation nuclei (CCN) by dissipating clouds at Palmer Station, Antarctica. *Geophys. Res. Lett.*, **23**, 69–72, <https://doi.org/10.1029/95GL03588>.
- Schlosser, E., F. A. Haumann, and M. N. Raphael, 2018: Atmospheric influences on the anomalous 2016 Antarctic sea ice decay. *Cryosphere*, **12**, 1103–1119, <https://doi.org/10.5194/tc-12-1103-2018>.
- Schmale, J., and Coauthors, 2013: Sub-Antarctic marine aerosol: Dominant contributions from biogenic sources. *Atmos. Chem. Phys.*, **13**, 8669–8694, <https://doi.org/10.5194/acp-13-8669-2013>.
- , and Coauthors, 2018: Long-term cloud condensation nuclei number concentration, particle number size distribution and chemical composition measurements at regionally representative observatories. *Atmos. Chem. Phys.*, **18**, 2853–2881, <https://doi.org/10.5194/acp-18-2853-2018>.
- Schmidt, A., K. S. Carslaw, G. W. Mann, A. Rap, K. J. Pringle, D. V. Spracklen, M. Wilson, and P. M. Forster, 2012: Importance of tropospheric volcanic aerosol for indirect radiative forcing of climate. *Atmos. Chem. Phys.*, **12**, 7321–7339, <https://doi.org/10.5194/acp-12-7321-2012>.
- Schmidt, K. M., S. Swart, C. Reason, and S.-A. Nicholson, 2017: Evaluation of satellite and reanalysis wind products with in situ wave glider wind observations in the Southern Ocean. *J. Atmos. Oceanic Technol.*, **34**, 2551–2568, <https://doi.org/10.1175/JTECH-D-17-0079.1>.
- Schutgens, N., S. Tsyro, E. Gryspeerd, D. Goto, N. Weigum, M. Schulz, and P. Stier, 2017: On the spatio-temporal representativeness of observations. *Atmos. Chem. Phys.*, **17**, 9761–9780, <https://doi.org/10.5194/acp-17-9761-2017>.
- Seinfeld, J., and S. N. Pandis, 2006: *Atmospheric Chemistry and Physics: From Air Pollution to Climate Change*. 2nd ed. Wiley-Interscience, 1152 pp.
- Sprenger, M., and H. Wernli, 2015: The LAGRANTO Lagrangian analysis tool – version 2.0. *Geosci. Model Dev.*, **8**, 2569–2586, <https://doi.org/10.5194/gmd-8-2569-2015>.
- Stephens, B. B., and Coauthors, 2018: The O<sub>2</sub>/N<sub>2</sub> Ratio and CO<sub>2</sub> Airborne Southern Ocean Study. *Bull. Amer.*

- Meteor. Soc.*, **99**, 381–402, <https://doi.org/10.1175/BAMS-D-16-0206.1>.
- Szczodrak, M., P. H. Austin, and P. B. Krummel, 2001: Variability of optical depth and effective radius in marine stratocumulus clouds. *J. Atmos. Sci.*, **58**, 2912–2926, [https://doi.org/10.1175/1520-0469\(2001\)058<2912:VOODAE>2.0.CO;2](https://doi.org/10.1175/1520-0469(2001)058<2912:VOODAE>2.0.CO;2).
- Trenberth, K. E., and J. T. Fasullo, 2010: Simulation of present-day and twenty-first-century energy budgets of the southern oceans. *J. Climate*, **23**, 440–454, <https://doi.org/10.1175/2009JCLI3152.1>.
- Turner, J., T. Phillips, G. J. Marshall, J. S. Hosking, J. O. Pope, T. J. Bracegirdle, and P. Deb, 2017: Unprecedented springtime retreat of Antarctic sea ice in 2016. *Geophys. Res. Lett.*, **44**, 6868–6875, <https://doi.org/10.1002/2017GL073656>.
- Twomey, S., 1959: The nuclei of natural cloud formation part II: The supersaturation in natural clouds and the variation of cloud droplet concentration. *Geofis. Pura Appl.*, **43**, 243–249, <https://doi.org/10.1007/BF01993560>.
- Twomey, S., 1977: The influence of pollution on the short-wave albedo of clouds. *J. Atmos. Sci.*, **34**, 1149–1152, [https://doi.org/10.1175/1520-0469\(1977\)034<1149:tiopot>2.0.co;2](https://doi.org/10.1175/1520-0469(1977)034<1149:tiopot>2.0.co;2).
- Vana, M., A. Virkkula, A. Hirsikko, P. Aalto, M. Kulmala, and R. Hillamo, 2007: Air ion measurements during a cruise from Europe to Antarctica. *Nucleation and Atmospheric Aerosols*, C. D. O’Dowd and P. E. Wagner, Springer, Eds., 368–372.
- Vehkamäki, H., M. Kulmala, I. Napari, K. E. J. Lehtinen, C. Timmreck, M. Noppel, and A. Laaksonen, 2002: An improved parameterization for sulfuric acid–water nucleation rates for tropospheric and stratospheric conditions. *J. Geophys. Res.*, **107**, 4622, <https://doi.org/10.1029/2002JD002184>.
- Vergara-Temprado, J., and Coauthors, 2018: Strong control of Southern Ocean cloud reflectivity by ice-nucleating particles. *Proc. Natl. Acad. Sci. USA*, **115**, 2687–2692, <https://doi.org/10.1073/pnas.1721627115>.
- Visakorpi, K., and Coauthors, 2018: Small-scale indirect plant responses to insect herbivory could have major impacts on canopy photosynthesis and isoprene emission. *New Phytol.*, **220**, 799–810, <https://doi.org/10.1111/nph.15338>.
- Wang, Z. B., and Coauthors, 2013: Long-term measurements of particle number size distributions and the relationships with air mass history and source apportionment in the summer of Beijing. *Atmos. Chem. Phys.*, **13**, 102159–102170, <https://doi.org/10.5194/acp-13-10159-2013>.
- Weingartner, E., S. Nyeki, and U. Baltensperger, 1999: Seasonal and diurnal variation of aerosol size distributions ( $10 < D < 750$  nm) at a high-alpine site (Jungfraujoch 3580 m asl). *J. Geophys. Res.*, **104**, 26 809–26 820, <https://doi.org/10.1029/1999JD900170>.
- Weller, R., K. Schmidt, K. Teinilä, and R. Hillamo, 2015: Natural new particle formation at the coastal Antarctic site Neumayer. *Atmos. Chem. Phys.*, **15**, 11 399–11 410, <https://doi.org/10.5194/acp-15-11399-2015>.
- Wernli, H., and H. C. Davies, 1997: A Lagrangian-based analysis of extratropical cyclones. 1. The method and some applications. *Quart. J. Roy. Meteor. Soc.*, **123**, 467–489, <https://doi.org/10.1002/qj.49712353811>.
- West, R. E. L., and Coauthors, 2014: The importance of vertical velocity variability for estimates of the indirect aerosol effects. *Atmos. Chem. Phys.*, **14**, 6369–6393, <https://doi.org/10.5194/acp-14-6369-2014>.
- Wiedensohler, A., and Coauthors, 2012: Mobility particle size spectrometers: Harmonization of technical standards and data structure to facilitate high quality long-term observations of atmospheric particle number size distributions. *Atmos. Meas. Tech.*, **5**, 657–685, <https://doi.org/10.5194/amt-5-657-2012>.
- Wofsy, S. C., 2011: HIAPER Pole-to-Pole Observations (HIPPO): Fine-grained, global-scale measurements of climatically important atmospheric gases and aerosols. *Philos. Trans. Roy. Soc. London*, **369A**, 2073–2086, <https://doi.org/10.1098/rsta.2010.0313>.
- Young, I. R., 1998: An intercomparison of GEOSAT, TOPEX and ERS1 measurements of wind speed and wave height. *Ocean Eng.*, **26**, 67–81, [https://doi.org/10.1016/S0029-8018\(97\)10016-6](https://doi.org/10.1016/S0029-8018(97)10016-6).
- Zheng, Y., D. Rosenfeld, and Z. Li, 2016: Quantifying cloud base updraft speeds of marine stratocumulus from cloud top radiative cooling. *Geophys. Res. Lett.*, **43**, 11 407–11 413, <https://doi.org/10.1002/2016GL071185>.
- Zhu, Y., D. Rosenfeld, and Z. Li, 2018: Under what conditions can we trust retrieved cloud drop concentrations in broken marine stratocumulus? *J. Geophys. Res. Atmos.*, **123**, 8754–8767, <https://doi.org/10.1029/2017JD028083>.
- Zieger, P., and Coauthors, 2017: Revising the hygroscopicity of inorganic sea salt particles. *Nat. Commun.*, **8**, 15883, <https://doi.org/10.1038/ncomms15883>.

An AMS Member Benefit

# MENTORING365

Support the Next Generation of Earth and Space Scientists



Developed in partnership with Earth and space science organizations, Mentoring365 provides mentors and mentees with structured relationship-building tools to develop and attain focused career goals.



**AMS**  
American Meteorological Society

[www.mentoring365.org](http://www.mentoring365.org)